International Journal of Heat and Mass Transfer 260 (2026) 128495

Contents lists available at ScienceDirect

International Journal of Heat and Mass Transfer

journal homepage: www.elsevier.com/locate/ijhmt

Experimental investigation of mixed convection in a horizontal tube for a liquid metal flow

Linda Elmlinger, Tim Laube, Benjamin Dietrich *, Thomas Wetzel

Institute of Thermal Process Engineering, Karlsruhe Institute of Technology (KIT), Kaiserstrasse 12, 76131 Karlsruhe, Germany

ARTICLE INFO

Keywords:
Liquid metal
Mixed convection
Gallium-indium-tin
Low-Prandtl number fluids
Buhr criterion
Nusselt correlation

ABSTRACT

An experimental study of the heat transfer on mixed convection in a turbulent liquid metal flow with azimuthally inhomogeneous heat flux distribution is presented. A horizontal nickel tube is heated in different sections to investigate the influence of heat flux orientation relative to gravity on heat transfer in a liquid metal flow. Four semi-circumferential heat flux distributions (top, bottom, right and bottom right half) are examined. These configurations emulate the azimuthally inhomogeneous heat flux profile that is characteristic of receiver tubes in concentrated solar power plants. The working fluid is a near eutectic alloy of gallium, indium, and tin (GaInSn, $Pr = 0.03$, $\vartheta_{melt} = 11°C$). The Péclet number is varied within a range of $2.4 \times 10^2 < Pe < 3 \times 10^3$, while the Rayleigh number is $1.6 \times 10^3 < Ra_q < 8.2 \times 10^3$. For all four heat flux distributions, the correlation for the azimuthally averaged Nusselt number $\langle Nu \rangle$ can be confirmed. The temperature difference along the circumference of the tube reveals mixed convection for heating directions opposing the direction of gravitational acceleration for $Pe < 7.2 \times 10^2$. Based on this quotient, the applicability of the Rayleigh number, the Buhr parameter, the Buoyancy parameter, and the Richardson number as criteria for the determination of mixed convection in liquid metals is discussed. New correlations for the critical Rayleigh number and limits for the Buhr parameter are established.

1. Introduction

Liquid metals are heat transfer fluids suitable for applications with high temperatures, high heat flux densities, and limited heat-exchange surfaces due to their superior heat conductivity compared to other liquids and gases [1,2]. Liquid metals commonly used as heat transfer fluid are sodium (Na), sodium-potassium (NaK), lead (Pb), and lead-bismuth eutectic (LBE) [3]. Established and developing applications are in fast breeder reactors [4] and nuclear fusion [5], for cooling electrical components [6], in high-temperature storage tanks [3], and in concentrated solar power plants (CSP) [1,2]. A CSP system with a central receiver system consists of numerous sun-tracking heliostats, which focus the sunlight onto a receiver at the top of a central tower. The receiver is made of multiple tubes arranged cylindrically around the top of the tower, which are heated from the outside by the concentrated sunlight and cooled from the inside by a heat transfer fluid. Common heat transfer fluids are superheated steam, molten salts, and liquid metals [7]. The fluid transfers its energy to the operating fluid of the power cycle e.g., via a steam generator. Due to the irradiance and the design of the receiver, the tubes are strongly heated from one side, while the other side remains cold. This non-uniform heat flux results in high thermal stresses which are increased by the cooling effect of the heat transfer fluid [8]. Additionally, mixed convection can occur when buoyancy induced by wall heat flux is of a comparable order of magnitude as inertial effects from the mass flow. Secondary flow effects caused by buoyancy can result in a distorted wall temperature distribution and changes in the local Nusselt number, resulting in unforeseen thermal stresses [9]. Those thermal stresses are important for the accurate life time prediction of receiver tubes subjected to varying heat fluxes throughout the daily operation [10]. Therefore, knowledge of possible mixed convection and local wall temperatures is essential for the correct mechanical design of the receiver [11].

However, a significant challenge arises when designing equipment for liquid metals as heat transfer fluids: the Reynolds analogy, which defines the similarity of temperature and velocity profile in a flow, is invalid. This results in a large discrepancy between the velocity and the temperature field of the flow [12]. Consequently, common Nusselt correlations for characterizing heat transfer based on the validity of the Reynolds analogy cannot be used for liquid metal flows [13–15]. The

* Corresponding author.
E-mail address: benjamin.dietrich@kit.edu (B. Dietrich).

https://doi.org/10.1016/j.ijheatmasstransfer.2026.128495
Received 16 September 2025; Received in revised form 2 February 2026; Accepted 5 February 2026
Available online 11 February 2026

Nomenclature

Latin symbols

B	buoyancy number $= 8 \times 10^4 \frac{Gr_q}{Re^{3.425}\, Pr^{0.8}}$ / -
c	coverage factor uncertainty / -
c_p	specific heat capacity at constant pressure / J kg^{-1} K^{-1}
D	diameter / m
g	gravitational acceleration / m s^{-2}
Gr	Grashof number $= \frac{g\ \beta\ \Delta T\ D_i^3}{\nu^2}$ / -
h	convective heat transfer coefficient / W m^{-2} K^{-1}
j	counter variable / -
k	thermal conductivity / W m^{-1} K^{-1}
L	length / m
$\dot{M}$	mass flowrate / kg s^{-1}
n	number of measurements / -
Nu	Nusselt number, $= \frac{h\ D_i}{k}$ / -
p	pressure / Pa
$\dot{Q}$	heat flux / W
$\dot{q}$	heat flux density / W m^{-2}
Pe	Péclet number, $= \frac{\rho\ c_p\ u\ D_{\mathrm{hyd}}}{k}$ / -
Pr	Prandtl number, $= \frac{\rho\ \nu\ c_p}{k}$ / -
R^2	coefficient of determination / -
Ra	Rayleigh number, $= Gr{\cdot}Pr$
Re	Reynolds number, $= \frac{4}{\pi}\frac{\dot{M}}{D_i\ \rho\ \nu}$ / -
Ri	Richardson number, $= \frac{Ra}{Re^2\ Pr}$ / -
r	radial coordinate / m
T	temperature / K
t	wall thickness / m
u	velocity / m s^{-1}
$\dot{V}$	volume flowrate / m^3 s^{-1}
x	referring to an arbitrary quantity
Z	Buhr parameter, $= \frac{Ra}{Re}\frac{D}{L}$ / -
z	axial coordinate / m

Greek symbols

β	thermal expansion coefficient / K^{-1}
ϑ	temperature / °C
θ	nondimensional temperature / -
μ	dynamic viscosity / Pa s
ν	kinematic viscosity / m^2 s^{-1}
ρ	density / kg m^{-3}
ϕ	azimuthal coordinate / °
ϕ^*	shifted azimuthal coordinate / °

Sub/-superscripts

Alloy201	selected nickel alloy
b	bulk
calm	calming length
center	center of heated side
crit	critical
heated	heated length
hyd	hydraulic length
i	inside
in	inlet
f	fluid
m	mean
max	maximum
melt	melting point
min	minimum
mp	measurement plane
Ni	Nickel
o	outside
out	outlet
q	heat flux
ref	reference
res	resulting
w	wall

Operators

$\langle\cdot\rangle$	azimuthal average
Δ	difference

Acronyms

CPS	concentrating solar power plant
GaInSn	gallium-indium-tin
GUM	Guide to the expression of Uncertainty in Measurement
HO	homogeneous heat flux
IHB	inhomogeneous heat flux from the bottom side
IHBR	inhomogeneous heat flux from the bottom right side
IHR	inhomogeneous heat flux from the right side
IHT	inhomogeneous heat flux from the top side
LBE	lead-bismuth eutectic
MAPE	mean absolute percentage error
Na	sodium
NaK	sodium-potassium
Pb	lead
PEEK	Polyetheretherketone
TC	thermocouple

objective of this work is to provide reliable Nusselt correlations and wall temperature profiles for a horizontal liquid metal tube flow. Numerical simulations can be validated using these data. Additionally, the study aims to identify the onset of mixed convection using correlations that can be applied during the design process of a receiver in a CSP system or other engineering equipment such as heat exchangers.

A previous study using the same test section and liquid metal circuit as in this work was conducted by Laube et al. [16]. The authors examined the azimuthally averaged Nusselt number $\langle Nu\rangle$ as a function of the Péclet number Pe for homogeneous heat flux in the range of $2.4 \times 10^2 < Pe < 3 \times 10^3$, resulting in the correlation given in Eq. (1)

$$\langle Nu_{\mathrm{Laube}}\rangle = 4.364 + 0.0276\ Pe^{0.803} \tag{1}$$

Although this correlation has been developed for data at homogeneous heat flux, it has been shown in [16], that it holds also for inhomogeneous heating. Further, the authors found that for inhomogeneous heating the azimuthal wall temperature distribution differs from the case of homogeneous heat flux, presenting a reduced inhomogeneity caused by the onset of secondary buoyancy flow for the case of inhomogeneous heating from the bottom side [17]. Their findings correspond with the results from numerous authors stating that concurrent free convection effects cause temperature and velocity profile distortion in both horizontally and vertically oriented heated tubes with turbulent liquid metal flows [18–21]. Buhr and Sesonske [9] studied the effect of mixed convection in a horizontal tube for a turbulent liquid metal flow ($2.9 \times 10^3 < Re < 1 \times 10^6$) by comparing five temperature distributions from other authors. The experimental setups consisted of a stainless-steel tube with an unheated calming section followed by a homogeneously heated section. Temperature patterns suggest that the secondary flow has a stagnation point at the highest point of the tube's cross-section, leading to wall temperature maxima. They concluded, that in a horizontal tube with constant heat flux, unexpected high

temperatures can arise when the design is based on mean or predicted Nusselt numbers. Zikanov et al. [15] investigated mixed convection flows in tubes and ducts with strong magnetic fields, varying the flow orientation and the heat flux distribution. In a horizontal tube heated at the bottom part without a magnetic field, a pair of axial convection rolls cause a reduced or even reversed streamwise velocity in the upper part of the tube. This results in a high temperature at the top section of the tube, confirming the aforementioned studies. Guo et al. [20] performed direct numerical simulations of mixed convection turbulent heat transfer in a horizontal channel with fluid properties of liquid lead. They observe stronger velocity fluctuations compared to the forced convection case, indicating the enhancement of turbulence with increasing influence of buoyancy. Additionally, secondary flow patterns arise depending on the direction of one-sided heating [22,23].

These studies highlight the complex interaction between buoyancy effects and turbulent flows, emphasizing the need to understand the underlying mechanisms of heat transfer when both forced and natural convection are present. This understanding is supported by the classification of heat transfer into free convection, mixed convection, and forced convection, as first proposed by Metais and Eckert [24]. They constructed flow regime maps for vertical and horizontal tubes based on liquids with $10^{-2} < Pr\ \frac{D_i}{L} < 1$. The maps show the Reynolds number Re versus $Gr\ Pr\frac{D_i}{L}$, where D_i is the inner tube diameter, L the length of the heated section of the tube, and Gr the dimensionless Grashof number. This number describes the ratio of buoyancy to viscous forces. The general definition of the Grashof number according to Eq. (2) includes the acceleration of gravity g, the thermal expansion coefficient of the fluid β_f, the temperature scale ΔT, the hydraulic length D_{hyd}, and the kinematic viscosity of the fluid ν_f.

$$Gr = \frac{g\ \beta_f\ \Delta T\ D_{hyd}^3}{\nu_f^2} \tag{2}$$

Further, the temperature scale depends on the heating rate. When heating is applied to the wall with a defined heat flux density $\dot{q}_w$, ΔT is calculated with Eq. (3)

$$\Delta T = \frac{\dot{q}_w\ D_{hyd}}{k_f} \tag{3}$$

D_{hyd} is the hydraulic length, and k_f is the thermal conductivity of the fluid. In the case of constant wall temperature of a tube, ΔT is defined as the difference between the wall surface temperature and the bulk temperature. Note that the definition of Gr and ΔT differs depending on the experimental setup and the author's preferences.

Other dimensionless numbers used for the characterization of mixed convection flows are the Rayleigh Ra and the Richardson number Ri, as defined in the nomenclature section. The Rayleigh number describes the heat transfer through natural convection and is defined as the product of the Grashof and the Prandtl number. The Rayleigh number is often used in definitions of other criteria like e.g., the Buhr parameter or the Richardson number. The Richardson number describes the ratio of buoyancy to inertia forces. In the case of conventional fluids with $Pr \approx 1$, the flow is considered to be in the forced convection regime for $Ri \ll 1$. For $Ri \gg 1$, the flow is dominated by forced convection [15]. Jackson et al. [19] have shown that buoyancy influences a vertical sodium flow for $Ri > 2 \times 10^{-3}$. For conventional fluids with $Pr \approx 0.7$, Sparrow et al. [25] concluded from their theoretical analysis of the boundary layer that mixed convection occurs for $Ri > 0.3$.

Buhr et al. [26] established a parameter for mixed convection derived from velocity and temperature field measurements in a sodium-potassium and a mercury flow, defined as the Buhr parameter according to Eq. (4)

$$Z = \frac{Ra}{Re}\ \frac{D_i}{L} \tag{4}$$

For this parameter, Ra is calculated using the temperature difference as in Eq. (5)

$$\Delta T = \frac{dT}{dz} D_i \tag{5}$$

The authors concluded from their measurements in vertical tubes with homogeneous heat flux, that mixed convection in liquid metal flows occurs for $Z > 2 \times 10^{-3}$. However, Gardner and Lykoudis [27] examined the temperature profiles of a mercury flow in a horizontal pipe with inhomogeneous heat flux and concluded, that the distortion of the temperature profiles indicates mixed convection for $Z > 1.2 \times 10^{-3}$. The experimental work of Laube [17] revealed mixed convection for $Z < 2 \times 10^{-3}$ as well. Given the discrepancies in the reported threshold values for the onset of mixed convection under inhomogeneous heat flux conditions, this work aims to critically assess the validity of the criterion proposed by Buhr et al. [26].

Another dimensionless number based on the Grashof number with ΔT from Eq. (3) is the Buoyancy number B according to Eq. (6).

$$B = 8 \times 10^4 \frac{Gr_q}{Re^{3.425}\ Pr^{0.8}} \tag{6}$$

This expression was developed by Hall and Jackson [28] and includes their suggestion, that buoyancy effects change the turbulence production due to the modification of the shear stress distribution across the pipe [29]. For this equation, the Dittus-Boelter equation for forced convective heat transfer has been used, which is only valid for medium-to-high Prandtl numbers. For $Pr \geq 0.7$, the influence of buoyancy forces can be neglected for $B < 3 \times 10^{-2}$, for $3 \times 10^{-2} < B < 3$ mixed convection effects are present, and for $B > 3$ free convection dominates [30]. Many authors use this expression for liquid metals although it is per definition, not applicable to low-Prandtl number fluids since the Dittus-Boelter equation only applies for fluids that satisfy the Reynolds analogy [31].

Jaeger and Hering [18] conducted a detailed review on publications on mixed convection with liquid metals and concluded that, in almost all publications, the information on the experiments is incomplete, lacks reproducibility, or exhibits additional inconsistencies, such as errors in the definition of dimensionless numbers. Furthermore, most of the experiments described in literature have been performed in the 1960s and 1970s, with natural limitations in instrumentation and uncertainty analyses as compared to today's standards. So, the mentioned shortcomings and limitations of existing data call for new experimental work to provide reliable Nusselt correlations for turbulent liquid metal flows in horizontal tubes under the influence of buoyancy effects. The present work aims to address these gaps by providing consistent and reproducible data for the analysis of buoyancy effects and the formulation of reliable Nusselt correlations for turbulent liquid metal flows in horizontal tubes.

2. Experimental setup

The test section and liquid metal circuit used in this work have already been described, validated and used in prior work [16] to determine the influence of the heat flux distribution on the heat transfer in a liquid metal flow in a horizontal tube. The flow is hydrodynamically fully developed and thermally developing [16]. Tests were carried out with homogeneous heating and inhomogeneous heating from either the top or the bottom section of the tube with an inlet temperature of $\vartheta_{in} = 25°C$. In the present work, the inlet temperature was reduced to $\vartheta_{in} = 17°C$ to obtain more data at lower Péclet numbers and examine the mixed convection regime. Additionally, two new boundary conditions (90° and 30° angle between the centerline of the heated half of the tube and the direction of gravitation) were established to acquire more information about the mixed convection regime and the influence of the heat flux distribution.

2.1. Heat transfer medium

The near eutectic alloy GaInSn (65.9 mass % gallium, 20.3 mass % indium, and 13.8 mass % tin) (MCP 11 from 5 N Plus UK Ltd.) is used as a working fluid. This alloy has a melting point of $\vartheta_{\mathrm{melt}} = 11°\mathrm{C}$ [32]. Further, it is non-toxic and presents a very low vapor pressure, making it a widely used laboratory fluid [33]. Its thermophysical properties are representative for a broad range of liquid metals and correlations for density, dynamic viscosity, specific heat capacity at constant pressure, and thermal conductivity are known (see Table 1). To prevent corrosion of the circuit's components, the maximum temperature of the fluid is limited to $\vartheta_{\mathrm{out}} = 50°\mathrm{C}$ [34].

2.2. Main circuit

Fig. 1 shows the experimental setup used to investigate mixed convection in a horizontal liquid metal flow.

The liquid metal circuit consists of a magnetically coupled centrifugal pump (Schmitt Kreiselpumpen GmbH & Co. KG, MPN190), a test section with a flow straightener (in-house construction), a static mixing element (NOV, KENICS 1-KMS-6), and a heat exchanger (in-house construction). A Coriolis sensor (Yokogawa Deutschland GmbH, Rotamass Prime 50) for measuring mass flowrate $\dot{M}$ and a magnetic-inductive flow sensor (KROHNE Messtechnik GmbH & Co. KG, Altoflux X1000) for measuring volume flowrate $\dot{V}$ are installed. Further, the liquid metal circuit includes various valves, pressure sensors (ICS Schneider Messtechnik GmbH, IMP321 and IMP331), and thermocouples (TCs) (Electronic Sensor GmbH, type K, 3 mm). During maintenance, the liquid metal is stored inside a storage tank. An expansion tank is installed at the circuit's highest point to compensate for fluctuating fluid levels during operation. The surface of the liquid metal is covered with argon gas to prevent its oxidation. Two filters (Alfred Durst Filtertechnik GmbH, polyethylene filter with a pore size of 20 µm) are installed in a bypass for the occasional removal of oxides and other particular impurities. A more detailed description of the circuit and its operation can be found in Laube et al. [16].

2.3. Test section

The test section consists of a tube with an inner diameter of $D_{\mathrm{i}} = 17.1$ mm and a wall thickness of $t = 1.25$ mm. The tube is made of nickel (Alloy 201) since high-nickel alloys display a high resistance against corrosion and are potential receiver materials [37]. Additional information on the material properties of Alloy 201 is included in Table 4 in Appendix A. A total of 70 TCs (Electronic Sensor GmbH, type K, 0.5 mm) are soldered into groves inside the tube wall at ten cross-sectional planes along the heated length of $L_{\mathrm{heated}} = 88.3\ D_{\mathrm{i}} = 1510$ mm at intervals of $\frac{L_{\mathrm{mp},j}}{D_{\mathrm{i}}} = [4.7,\ 9.3,\ 14,\ 18.7,\ 28.1,\ 37.4,\ 46.8,\ 56.1,\ 65.5,\ 74.8]$. Twelve TCs each are mounted in five measuring planes $\left(\frac{L_{\mathrm{mp},j}}{D_{\mathrm{i}}} = [\ 18.7,\ 37.4,\ 56.1,\ 65.5,\ 74.8]\right)$ at azimuthal intervals of $\Delta\phi = 30°$ around the circumference of the tube as shown in Fig. 2.

Inside the remaining measuring planes, one TC at the top ($\phi = 90°$) and one at the bottom ($\phi = 270°$) are installed. The outer surface of the tube is covered with a gapfiller (HALA Contec GmbH & Co. KG, TEL-Z-SI) to ensure complete thermal contact with the six surrounding heating segments along its circumference and axial length. Six electrical heaters (Thermocoax Isopad GmbH, ZEZAc40) are embedded in each of the aluminum heating segments, totaling up to 36 electrical heaters. Each heating segment is separated from the adjacent heating segments by PEEK spacers and can be heated differently using individually adjustable power controllers (Advanced Energy Industries Inc., Thyro PX and JUMO GmbH & Co. KG, TYA 201). This allows the various boundary conditions shown in Fig. 3 to be set. The conditions are homogeneous heat flux (HO), inhomogeneous heat flux from the top side (IHT), inhomogeneous heat flux from the bottom side (IHB), inhomogeneous heat flux from the right side (IHR), and inhomogeneous heat flux from the bottom right side (IHBR). The last two conditions result from a 30° axial rotation of the entire test section.

Measurement grids containing eight TCs (Electronic Sensor GmbH, type K, 0.5 mm) are mounted at the inlet and outlet of the test section to determine the inlet and outlet bulk temperature of the liquid metal flow. A calming section with a length of $L_{\mathrm{calm}} = 37.4\ D_{\mathrm{i}} = 640$ mm is installed at the entrance of the heated section to ensure that the flow is fully developed before entering the heated section. Heaters, tubes, valves, and TC plugs are insulated to prevent heat losses and input from the periphery. A brief consideration of the aging effects of the test section is included in Appendix B.

Table 1
Physical properties of GaInSn.

Physical property	Correlation	Uncertainty
Density [32]	$\frac{\rho_{\mathrm{GaInSn}}(T)}{\mathrm{kg\ m^{-3}}} = -0.758\ \frac{T}{\mathrm{K}} + 6637.9$	± 0.06 %
Dynamic viscosity [35]	$\frac{\mu_{\mathrm{GaInSn}}(T)}{\mathrm{Pa\ s}} = 4.352 \times 10^{-4} \exp\left(\frac{3904}{8.3144\ \frac{T}{\mathrm{K}}}\right)$	± 4 %
Specific heat capacity at constant pressure [36]	$\frac{c_{p,\mathrm{GaInSn}}(T)}{\mathrm{J\ kg^{-1}K^{-1}}} = 6.67 \times 10^{-6}\frac{(T - 273.15\ \mathrm{K})^2}{\mathrm{K}^2} - 0.11\frac{(T - 273.15\ \mathrm{K})}{\mathrm{K}} + 368.01$	± 5 % *
Thermal conductivity [35]	$\frac{k_{\mathrm{GaInSn}}(T)}{\mathrm{W\ m^{-1}K^{-1}}} = 4.9 \times 10^{-5}\frac{(T - 283.7\ \mathrm{K})^2}{\mathrm{K}^2} + 0.0614\frac{(T - 283.7\ \mathrm{K})}{\mathrm{K}} + 23.4$	± 7 %

*This value is estimated since the authors do not state any uncertainty.

2.4. Uncertainty analysis

An uncertainty analysis following the instructions given in the "Guide to the expression of Uncertainty in Measurement" (GUM) [38] was carried out. A type B evaluation of standard uncertainty was performed using a coverage factor of $c = 2$ and a level of confidence of 95%. The flow meters and pressure sensors are factory-calibrated. All loose TCs were calibrated using a reference thermometer (Isothermal Technology Limited, Isotech SPRT 909 L/25/TTI with Isotech milliK) and the TCs inside the test section were calibrated in-situ after installation. Further, the uncertainties of the physical properties of the test fluid (see Table 1) are included in the analysis. The test section and the method of measurement have been validated using water as test fluid in prior work [16]. The values obtained for Nusselt number and friction factor of a turbulent water flow agree with the well-established correlation by Gnielinski [39]. A more detailed explanation can be found in the work by Laube et al. [16].

3. Data analysis

The physical properties of GaInSn are calculated with the correlations given in Table 1 at the mean bulk temperature of the fluid $T_{\mathrm{b,m}} = \frac{1}{2}\left(T_{\mathrm{b,in}} + T_{\mathrm{b,out}}\right)$ inside the test section. The mean temperature is calculated from the fluid's inlet $T_{\mathrm{b,in}}$ and outlet $T_{\mathrm{b,out}}$ bulk temperatures, which are measured by the measurement grids at the respective locations.

The physical properties of the test fluid are characterized by the Prandtl number. The combination of Prandtl and Reynolds number represents the ratio of thermal energy transported by convection

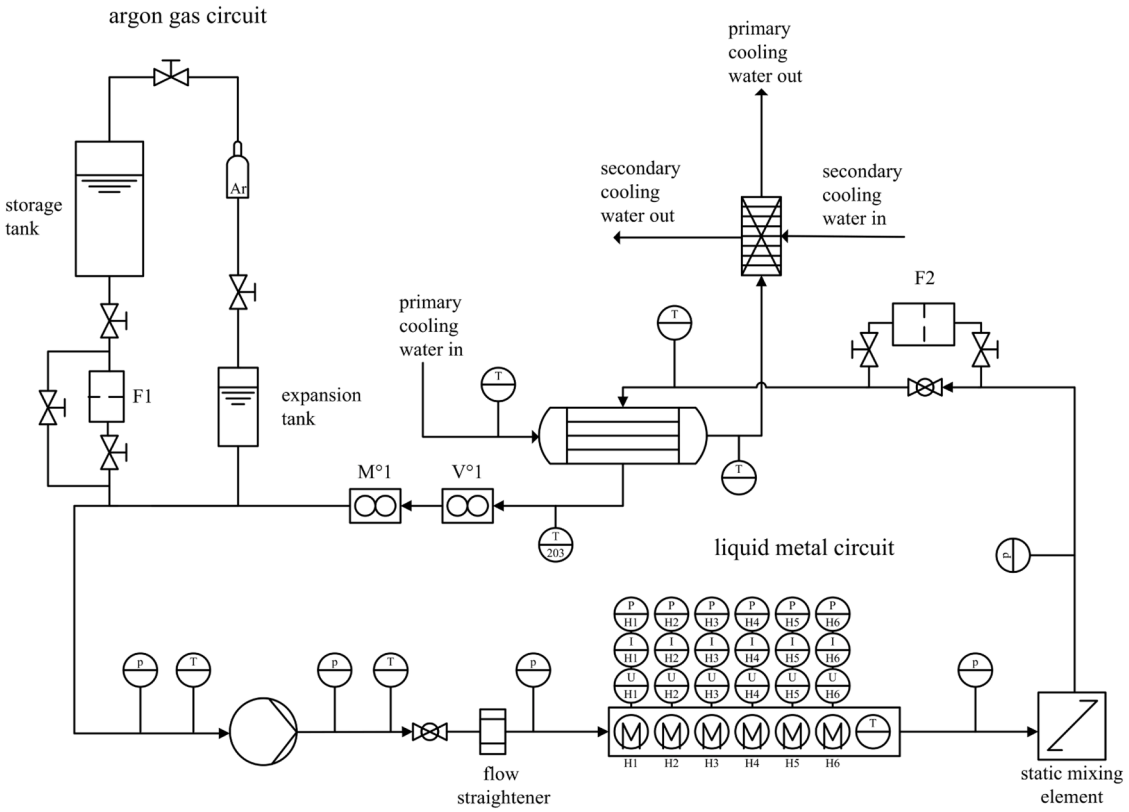

Fig. 1. Schematic of the experimental setup [16], with changes.

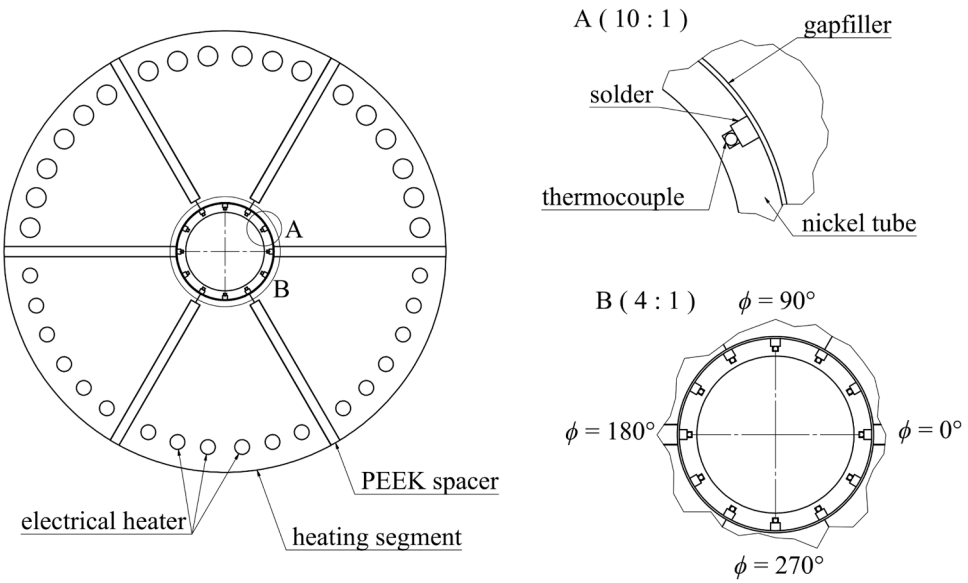

Fig. 2. Cross-section of the test section and heating segments with details on the positions of TCs.

$(\rho_f\ u\ c_{p,f})$ and by molecular conduction (k_f/D_{hyd}), and is called the Péclet number *Pe*. The definitions of *Pr* and *Pe* are included in the nomenclature section. For this work's experimental setup, the Reynolds number *Re* is defined by Eq. (7).

$$Re = \frac{4\,\dot{M}}{\pi\,D_i\,\rho_f\,\nu_f} \tag{7}$$

ρ_f is the density of the fluid. Using the definition of the dimensionless numbers mentioned before, the Buhr criterion (see Eq. (4)) is defined as given in Eq. (8).

$$Z = \frac{D_i^6\,\pi\,g\,\beta_f\,(T_{out} - T_{in})\,c_{p,f}\,\rho_f^2}{4\,\dot{M}\,k_f\,L_{heated}^2} \tag{8}$$

$c_{p,f}$ the specific heat capacity at constant pressure. For the evaluation of mixed convection based on *Ra*, the definition of the Grashof number (see Eqs. (2) and (3)) result in Eq. (9).

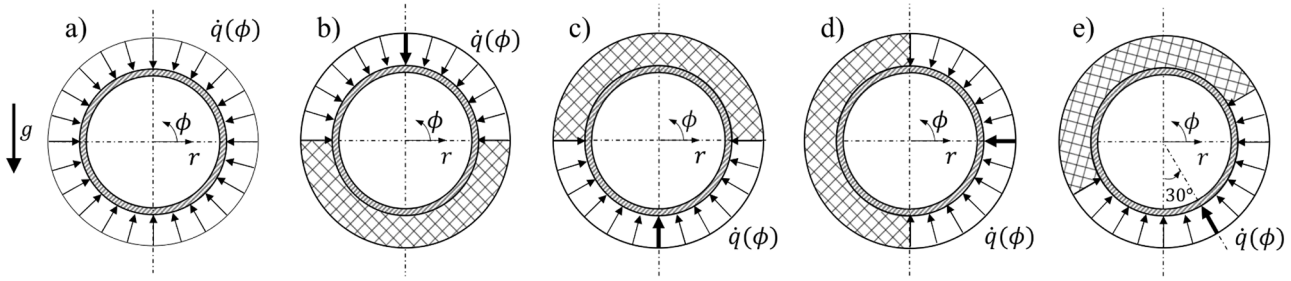

Fig. 3. Thermal boundary conditions in the test section. The conditions are a) homogeneous heat flux (HO), b) inhomogeneous heat flux from the top side (IHT), c) inhomogeneous heat flux from the bottom side (IHB), d) inhomogeneous heat flux from the right side (IHR), and e) inhomogeneous heat flux from the bottom right side (IHBR). The center of the heated side ϕ_{center} is marked bold.

$$Ra = \frac{g\,\beta_\text{f}\,\dot{q}_\text{w}\left(\frac{D_\text{i}}{2}\right)^4 \rho_\text{f}^2\,c_{p,\text{f}}}{k_\text{f}^2\,\mu_\text{f}} \tag{9}$$

Here, the hydraulic length is defined as half of the tube diameter, as suggested in [40], since the heat is transferred through half of the tube's surface for the heating conditions examined in this work. μ_f is the dynamic viscosity. The circumferential local convective heat transfer coefficient $h(\phi,z)$ is defined in Eq. (10).

$$h(\phi,z) = \frac{\dot{q}_\text{w}(\phi,z)}{T_\text{w}(\phi,z) - T_\text{b}(z)} \tag{10}$$

$T_\text{w}(\phi,z)$ is the local temperature and $\dot{q}_\text{w}(\phi,z)$ the local heat flux density at the inner surface of the tube. ϕ is the circumferential position and z the axial position along the tube. The local bulk temperature $T_\text{b}(z)$ is calculated with Eq. (11).

$$T_\text{b}(z) = \frac{\dot{Q}_\text{res}}{\dot{M}\,c_{p,\text{f}}}\,\frac{z}{L_\text{heated}} + T_\text{b,in} \tag{11}$$

The resulting heat input rate $\dot{Q}_\text{res}$ is derived from an energy balance around the fluid inside the test section and is calculated by Eq. (12).

$$\dot{Q}_\text{res} = \dot{M}\,c_{p,\text{f}}\,\left(T_\text{b,out} - T_\text{b,in}\right) \tag{12}$$

For the calculation of $\dot{q}_\text{w}(\phi,z)$, a distinction must be made, depending on the heating condition. For the case of homogeneous heat flux, the heat flux density at the inner wall of the tube is calculated by Eq. (13).

$$\dot{q}_\text{w,HO} = \frac{\dot{Q}_\text{res}}{L_\text{heated}\,\pi\,D_\text{i}} \tag{13}$$

More complex calculations are necessary for the case of inhomogeneous heat flux due to the azimuthal heat conduction inside the tube wall. This method is inspired by Schmidt and Sparrow [40]. The local temperatures inside the tube wall $T_\text{w,TC}(\phi,z)$ are measured by TCs around the circumference of the tube. A Fourier series with five harmonics is fitted to the data to obtain the continuous function $T(\phi)_\text{TC}$ at each measuring plane. This function is used as boundary condition for solving the two-dimensional Laplace heat conduction equation in cylindrical coordinates without volumetric heat source (see Eq. (14)).

$$\frac{1}{r}\frac{\partial}{\partial r}\left(r\frac{\partial T}{\partial r}\right) + \frac{1}{r^2}\frac{\partial^2 T}{\partial \phi^2} = 0 \tag{14}$$

Here, r is the radial coordinate. To solve this homogeneous partial differential equation, the following assumptions are made:

- The heat conduction is considered to be two-dimensional, because the temperature gradient in axial direction is negligible small compared to the radial and azimuthal temperature gradient in the tube wall.
- The heat flux density on the outer surface of the tube $\dot{q}_\text{w}$ is constant along its entire length, as the heat within each heating element is uniformly distributed across the entire segment.
- The physical properties of tube material are calculated using the mean wall temperature at the measurement plane under consideration.
- Any distortions of the temperature field by the TCs soldered into the grooves in the tube wall are neglected.

The temperature profile at the outer surface of the tube is calculated with the thermal conductivity of the nickel alloy k_Ni using Eq. (15).

$$\frac{\partial T}{\partial r}(r = r_\text{o}, \phi) = \frac{\dot{q}_\text{o}}{k_\text{Ni}} \tag{15}$$

The heat flux density at the outside of the tube $\dot{q}_\text{o}$ is defined in segments according to the applied heating condition illustrated in Fig. 3. Solving Eq. (14) with Eq. (15) as a constant heat flux boundary condition at the outside of the tube and the approximated temperature function $T(\phi)_\text{TC}$ as constant temperature boundary condition for each measuring plane results in the temperature distribution at the inner surface of the tube $T_\text{w}(\phi,\ z)$. The heat flux density at the inner wall is then calculated through the Fourier law stated in Eq. (16).

$$\dot{q}_\text{w} = k_\text{Ni}\frac{\partial T}{\partial r}\bigg|_{r=r_\text{i}} \tag{16}$$

The uncertainty analysis includes the differences between the analytical solution of the Laplace heat conduction equation and numerical simulations.

The azimuthally averaged Nusselt number is defined as given in Eq. (17).

$$\langle Nu\rangle = \frac{\dot{q}_\text{w}(\phi,\ z)\,D_\text{i}}{(T_\text{w}(\phi,\ z) - T_\text{b}(\phi,z))\,k_\text{f}} \tag{17}$$

For the comparison of wall temperatures at different directions of heating and inlet temperatures, the dimensionless temperature θ introduced by Schmidt and Sparrow [40] as stated in Eq. (18) is used.

$$\theta = \frac{T_\text{w}(\phi,z) - T_\text{b}(z)}{\langle T_\text{w}(\phi,z)\rangle - T_\text{b}(z)} \tag{18}$$

The mean absolute percentage error (MAPE) with its definition given in Eq. (19) is used to calculate the difference between experimental results and a reference.

$$\text{MAPE} = \frac{100\ \%}{n}\sum_{i=1}^{n}\left|\frac{x_\text{ref} - x_1}{x_\text{ref}}\right| \tag{19}$$

x_ref is the corresponding reference, x_1 is the measured quantity, and n is the number of measurements.

4. Results and discussion

The test conditions are summarized in Table 2. For all the evaluations shown, the data from the measurement plane at the heated length of $L_{mp,9} = 65.5\ D_i = 1120.05$ mm, which contains twelve TCs, have been taken. Previous studies [16,41] with the identical test section suggest that the flow can be assumed to be thermally fully developed at the measurement plane used [42]. The data of the heating conditions IHT and IHB with $\vartheta_{in} = 25°C$ are taken from the published data set from Laube et al. [43].

4.1. Nusselt number

Fig. 4 shows the azimuthally averaged Nusselt number $\langle Nu \rangle$ versus the Péclet number Pe for inhomogeneous heat flux from the top side (IHT) and bottom side (IHB) at different heat flux densities and inlet temperatures.

$\langle Nu \rangle$ increases with increasing Pe and does not show a dependency on heat flux density. For both IHT and IHB, $\langle Nu \rangle$ falls within the respective uncertainty of measurement. This suggests that the orientation of heating exerts no discernible influence on $\langle Nu \rangle$. The additional data recorded at an inlet temperature of $\vartheta_{in} = 17°C$ allows for the investigation of liquid metal flow at lower Pe and higher heat fluxes without exceeding the maximum outlet temperature $\vartheta_{out} = 50°C$. Compared to the Nusselt correlation Nu_{Laube} based on homogeneous heating (HO) given in Eq. (1), $\langle Nu \rangle$ increases for inhomogeneous heating from one side, but remains within the 20 % deviation, which corresponds to the confidence interval of the correlation [16]. The transferability of correlations with homogeneous heating to inhomogeneous heating is confirmed by other authors [8,41,44]. Therefore, $\langle Nu \rangle$ and consequently, the azimuthally averaged heat transfer coefficient h for inhomogeneous heat flux from the top and bottom side can be determined with Eq. (1).

As shown in Fig. 5, $\langle Nu \rangle$ versus Pe for inhomogeneous heat flux from the right side (IHR) and the bottom right side (IHBR) can be described by the Nusselt correlation for HO for $Pe \gtrsim 400$ as well. In this Péclet range, 88 % of the data points for IHB and 95 % of the data points for IHBR fall within the 20 % deviation of the Nusselt correlation Nu_{Laube} of Laube et al. [16]. However, for $Pe \lesssim 400$, the agreement with Nu_{Laube} decreases since none of the data points for IHB and only 50 % for IHBR are within the 20 % deviation. Therefore, the correlations presented in Appendix C may be considered a more suitable alternative for describing $\langle Nu \rangle$ for $Pe \lesssim 400$. Note that $\langle Nu \rangle$ for small Pe is smaller for the case of IHR and IHBR compared to IHB and IHT, indicating a decreased heat transfer. An influence of heat flux density is not visible for any of the data shown.

The local Nusselt number at the center of the heated side ϕ_{center} (marked in Fig. 3) is overestimated for all directions of heating when the correlation Nu_{Laube} is used as shown in Fig. 6.

An overestimation of $Nu(\phi_{center})$ directly translates into an overestimation of the local heat transfer coefficient $h(\phi_{center})$. Based on this, predictions of the local wall temperature $T_w(\phi, z)$ result in underestimated values. This can cause unforeseen peak thermal stresses in the wall, that may lead to permanent plastic deformation and eventual failure [11]. The discrepancy, particularly for IHB and IHBR, could be caused by buoyancy effects, which are not sufficiently captured by correlations for $\langle Nu \rangle$. To better understand these effects on the local wall temperature distribution, the dimensionless temperature θ (see Eq. (18)) should be considered more closely.

Table 2
Operation conditions of experiments with GaInSn.

Quantity	Dimension	Value
Inlet temperature ϑ_{in}	°C	17, 25
Heat flux density $\dot{q}_w$	kW m^{-2}	46 - 110
Prandtl number Pr	-	0.03
Reynolds number Re	-	$8 \times 10^3 - 10^5$
Péclet number Pe	-	$240 - 3{,}000$

4.2. Dimensionless temperature

Comparing θ at the inner surface of the tube along the circumference for inhomogeneous heating at different heat flux densities and high Reynolds numbers $(Re > 5 \times 10^4)$ does not show any dependency of θ from the heat flux density or heating condition, as expected from theoretical considerations [45]. No difference between the data sets can be determined since the heat transfer mechanism is forced convection only. Instead, the comparison of θ at $Pe = 430$ for all four heat flux distributions shown in Fig. 7 demonstrates the influence of the heat flux distribution on θ.

For better comparability, ϕ is shifted so the heated section is located at $0° < \phi^* < 180°$ for all heating conditions. The dimensionless temperatures for the different inhomogeneous heat flux distributions deviate significantly from unity as detected for HO [17]. This circumstance can be explained with regard to the temperatures of the wall and the fluid close to the wall. In liquid metal flows with half-sided heating, the fluid temperature near the unheated tube wall tends to be considerably lower than the mass-averaged temperature of the bulk flow [46]. For the data range examined in the present work, the maximum temperature difference between the heated and the unheated sides is $\Delta T = 15.6$ K ($\dot{q}_w = 110$ kW m^{-2}, $Pe = 462$). Fig. 7 also clearly shows that θ depends on the direction of heat flux. The values of θ for IHB and IHT are higher than those for IHB and IHBR, both on the heated and unheated sides. The differences between the different heat flux distributions are not caused by inhomogeneity in the heating segments, since temperature measurements inside the heating segments confirm that they are identical. A plausible explanation for the dependency of θ on the heat flux distribution would be a change of flow pattern under the influence of buoyancy effects. At high Reynolds numbers, no dependency of the dimensionless temperature on the heat flux is observed, presumably because no buoyancy effects occur and only forced convection dominates. In contrast, at small Reynolds numbers as shown in Fig. 8, a dependency of θ from the heat flux density is distinguishable for all heating conditions except for IHT. This suggests that mixed convection may not occur when the heat flux distribution is opposite to the buoyancy direction in a horizontal tube. In the literature, this case is commonly referred to as stably stratified. Mixed convection may occur in the case of unstable stratification (IHT), neutral stratification (IHR), and partially unstable stratification (IHBR).

This finding agrees with the work of Schmidt and Sparrow [40], who could not detect mixed convection in a horizontal tube flow of water when heated from the top side. Further, Fig. 8 shows the asymmetry of θ to the vertical mirror axis of the cross-section (at $\phi = 30°$ for IHR and at $\phi = 330°$ for IHBR) and emphasizes the directionality of the mixed convection effects. Xu et al. [47] simulated the heat transfer of a horizontal tube flow of supercritical CO_2 under a non-uniform heat flux profile applied over 240° of the tube's circumference. The authors conclude, that the orientation of the downward flow in the center along the direction of gravity and the size of the two vortices to the side of the downward flow depends on the orientation of the heating. For the cases that the heating center was located on the top side of the tube and on the bottom side, the flow pattern is mirrored by the gravitational direction, but the intensity of secondary flow is less pronounced for the case of heat flux from the top. This is in accordance with the assumption of absence of mixed convection at IHT in the present work. Further, the flow pattern simulations derived from side heating in [47] shows that for all heat flux distributions, the hot and therefore less dense fluid close to the wall rises, cools off, and then flows down in the center. In the present work, the flow patterns for IHR and IHBR are presumably different from IHT and IHB since the vortices are neither mirror-symmetrical nor identical in size and shape. The different flow patterns may result in different

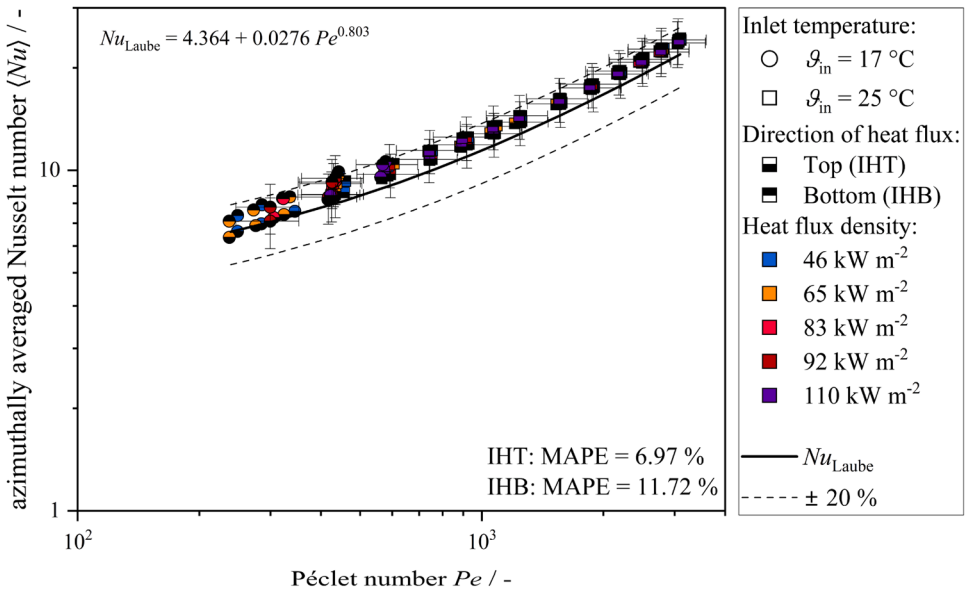

Fig. 4. Azimuthally averaged Nusselt number ⟨*Nu*⟩ versus Péclet number *Pe* for IHT and IHB at different heat flux densities. The exemplary uncertainty of measurement for $\dot{q}_w = 92$ kW m^{-2} is shown for both heat flux distributions.

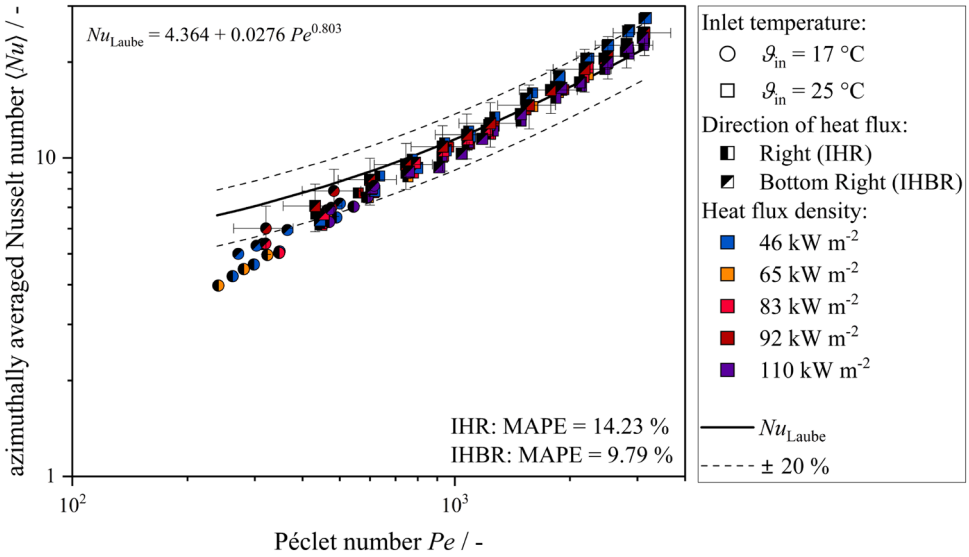

Fig. 5. Azimuthally averaged Nusselt number ⟨*Nu*⟩ versus Péclet number *Pe* for IHR and IHBR at different heat flux densities. The exemplary uncertainty of measurement for $\dot{q}_w = 92$ kW m^{-2} is shown for both heat flux distributions.

temperature distributions along the circumference of the tube and consequently, asymmetrical dimensionless temperatures [47].

The biggest difference between θ for different heat flux densities appears at the center of the heated side for each direction of heating, as illustrated in Figs. 7 and 8. Therefore, a comparison of the maximum and minimum of θ for each heating condition with selected heat flux densities is shown in Fig. 9. The complete presentation of all data from θ_{max} and θ_{min} is included in Figs. 20 and 21, which can be found in Appendix D.

The curves of θ_{max} and θ_{min} are symmetrical around a mirror axis at $\theta = 1$. Therefore, conclusions based on θ_{max} are transferable onto θ_{min}. All data sets of θ_{max} as a function of *Pe* exhibit a similar trend: After an initial steep increase with increasing *Pe*, θ_{max} reaches a maximum. With further increasing *Pe*, θ_{max} displays a gradual decrease. Due to the slight inconsistency regarding the exact position of the TCs inside the wall at $\phi = 90°$ and $\phi = 270°$, the data for IHT and IHB shows a distinct offset, but still remains within the coverage area of the uncertainty intervals of θ_{max} and θ_{min}.

At small *Pe*, θ_{max} increases, meaning that the inhomogeneity of the wall temperature distribution increases with increasing *Pe*, until a maximum is reached. In this region, an increase in *Pe* may result in a reduction of the convective heat transfer resistance compared to the azimuthal thermal heat conduction resistance in the wall. This presumably results in higher inhomogeneity of the wall temperature distribution. With further increase of *Pe*, θ_{max} decreases and the wall temperature distribution is more homogeneous due to an additional heat transfer path in the fluid which is more pronounced due to the higher rate of turbulence of the flow [17].

Both θ_{max} and θ_{min} resulting from the IHR and IHBR are closer to unity, meaning that the inhomogeneity of the inner surface temperature of the tube at the highest respectively the lowest point of circumference is smaller than for the other heating conditions although the heat flux

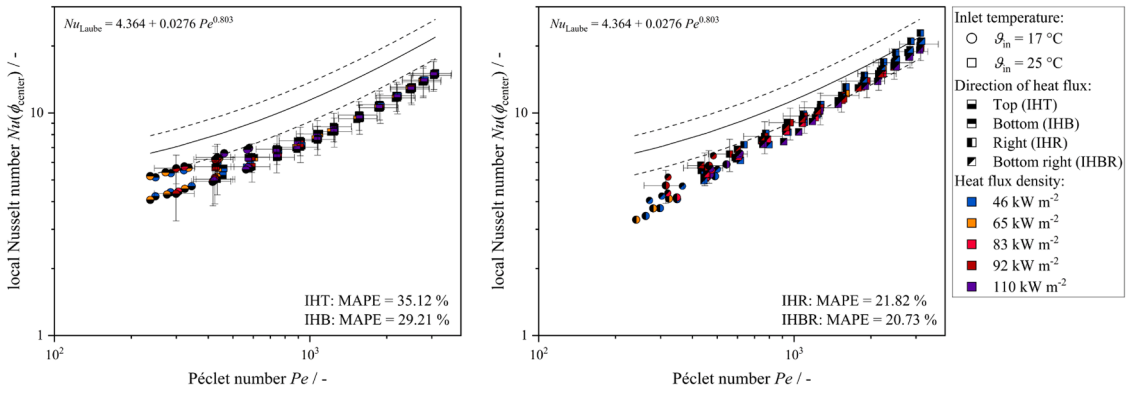

Fig. 6. Local Nusselt number $Nu(\phi_{center})$ at the center of the heated side ϕ_{center} versus Péclet number Pe at different heat flux densities for all four heat flux distributions. The exemplary uncertainty of measurement for $\dot{q}_w = 92$ kW m^{-2} is shown for all heat flux distributions.

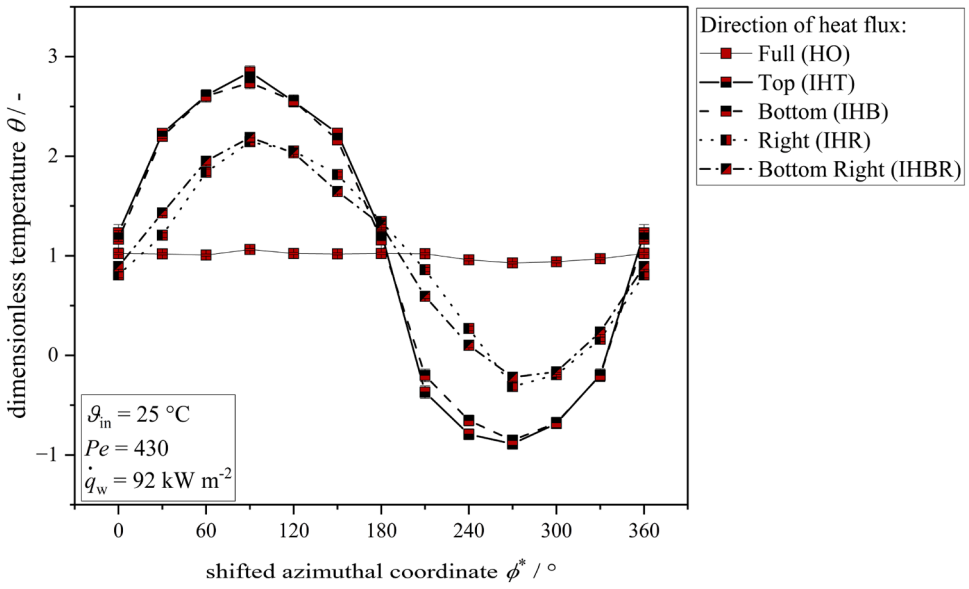

Fig. 7. Dimensionless temperature $\boldsymbol{\theta}$ versus the shifted azimuthal coordinate ϕ^* at heat flux of $\dot{q}_w = 92$ kW m^{-2} and different directions of heating. The uncertainty of measurement is included but covered by the data symbols.

density and mass flowrate are identical. Interestingly, this behavior represents the same characteristics as $\langle Nu \rangle$, which is lower for all data from IHR and IHBR compared to IHT and IHB. The decrease of θ_{max} respectively the increase of θ_{min} for increasing Pe is not as pronounced for IHBR as for the other heating conditions. This could be explained with a lower influence of turbulence on the heat transfer in the investigated flow regime for IHBR, since the influence of molecular heat conduction on heat transfer is more pronounced than the influence of turbulence in liquid metals [42].

To rule out that the decrease of θ_{max} with increasing Pe results from a change in the thermal conductivity of the tube material instead from the increased rate of turbulence, k_{Ni} is calculated for exemplary data sets at different flow and heating conditions, summarized in Table 3.

Table 3 shows that the thermal conductivity of the tube wall is increased for an increase in Re due to the decreased temperature at the inner surface of the tube. The thermal conductivity increases about $\Delta k_{Ni} = 0.6$ % while the maximum dimensionless temperature decreases up to $\Delta\theta_{max} = 7$ % depending on the direction of heating. Therefore, the homogenization of the wall temperature and consequently, the decrease of θ_{max} with increasing Pe is rather be expected to be the result of the rising turbulence rate of the flow. This means in essence, that the wall temperatures homogenize due to the heat transport in the fluid from the heated to the unheated side.

For a more detailed investigation of the influence of buoyancy effects on the heat transfer in the fluid, θ_{max} is examined more closely. The quotient $\frac{\theta_{max,IHT}}{\theta_{max,IHB}}$ is used to compare the maxima of the dimensionless temperatures to show the difference between the direction of heating for IHT and IHB, shown in Fig. 10.

At high Pe, the quotient does not depend on the heat flux density and therefore, the flow is dominated by forced convection only. Due to the individual characteristics of the TCs discussed before, the quotient approaches 0.94 for forced convection at high Pe. Considering the measurement uncertainty of the TCs, the values with $\theta_{max,IHT}/\theta_{max,IHB} > 0.99$ are deemed to be influenced by mixed convection effects. This value also corresponds to the 5 % criterion introduced by Schmidt and Sparrow [40] and reveals mixed convection for the present data at $Pe < 7.2 \times 10^2$, depending on the heat flux density.

Comparing θ_{max} of IHR and IHBR with IHT leads to different results. The quotient does not reach $\theta_{max,IHT}/\theta_{max,IHR} = 0.94$ for $Pe \to \infty$ since all θ_{max} for IHT are larger than for IHR and IHBR as i.e., shown in Fig. 9a. Due to the difficulty of comparing the data mentioned, other criteria for the onset of mixed convection are considered.

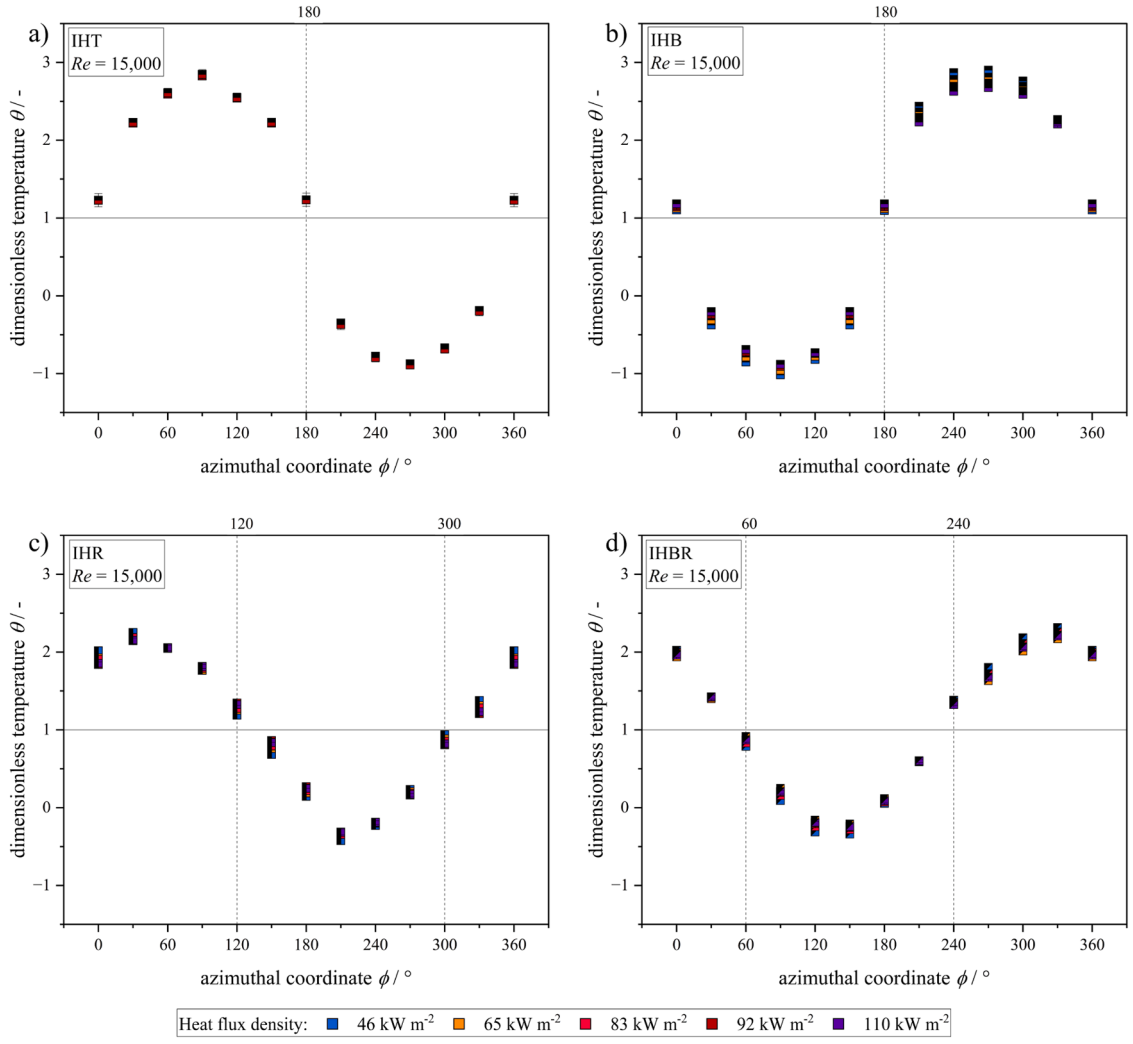

Fig. 8. Dimensionless temperature $\boldsymbol{\theta}$ versus azimuthal coordinate ϕ for a) inhomogeneous heat flux from the top side, b) inhomogeneous heat flux from the bottom site de, c) inhomogeneous heat flux from the right side, and d) inhomogeneous heat flux from the bottom right side. The exemplary uncertainty of measurement for $\dot{q}_w = 92$ kW m^{-2} is included, but covered by the data symbols. The boundaries of the heated and unheated sides are marked with dashed lines.

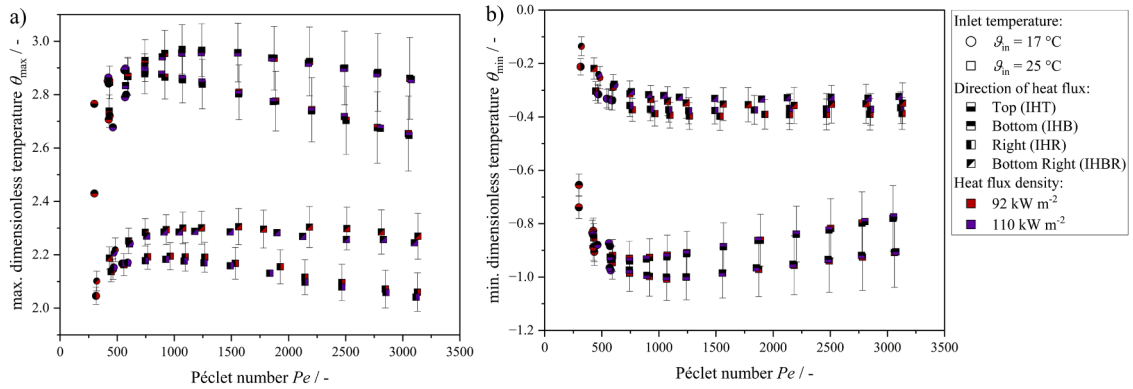

Fig. 9. Comparison of a) maximum of dimensionless temperature θ_{max} and b) minimum of dimensionless temperature θ_{min} versus Péclet number Pe for different heating conditions and heat flux densities. The exemplary uncertainty of measurement for $\dot{q}_w = 92$ kW m^{-2} is shown.

Table 3
Comparison of the change of thermal conductivity $\boldsymbol{k_{Ni}}$ of the tube wall and the maximum local dimensionless wall temperatures $\boldsymbol{\theta_{max}}$ for different directions of heating at identical heat flux density of $\dot{\boldsymbol{q}}_{\mathbf{w}} = 92$ **kW m**$^{-2}$ and two different Reynolds numbers ***Re***.

Direction of heat flux	Re / -	$\langle T_{w,i} \rangle$ / K	k_{Ni} / W m^{-1}K^{-1}	θ_{max} / -
Top (IHT)	3×10^4	309.46	74.54	2.87
	10^5	302.35	75.00	2.68
Bottom (IHB)	3×10^4	309.89	74.51	2.95
	10^5	302.58	74.98	2.86
Right (IHR)	3×10^4	308.63	74.59	2.19
	10^5	301.91	75.03	2.06
Bottom Right (IHBR)	3×10^4	308.47	74.60	2.29
	10^5	302.02	75.02	2.27

4.3. Criteria for mixed convection

The widely known flow regime maps by Metais and Eckert cannot be used for the present data as the data for GaInSn does not fall within the scope of validity of $10^{-2} < Pr\ \frac{D_i}{L} < 1$. As discussed earlier, there are several dimensionless numbers to characterize the convection regime, but they have different definitions depending on the orientation applied. Nevertheless, the Rayleigh number [40], the Buhr parameter [26], the Buoyancy parameter [29], and the Richardson number [15] are applied, focusing on the data under the influence of mixed convection indicated by $\theta_{max,IHT}/\theta_{max,IHB} > 0.99$.

4.3.1. Rayleigh number

Based on $\theta_{max,IHT}/\theta_{max,IHB} > 0.99$ for flow and heating conditions in the mixed convection regime, a new correlation for the critical Rayleigh number $Ra_{q,crit}$ is developed. Ra_q is the Rayleigh number calculated with the Grashof number at constant heat flux density (see Eq. (9)). According to literature [40], the hydraulic length is defined as $D_{hyd} = \frac{D_i}{2}$ and the heat flux density at the inner surface is the mean heat flux density at the heated side. For $Ra_q > Ra_{q,crit}$ buoyancy effects occur and influence heat transfer. A flow with $Ra_q < Ra_{q,crit}$ is not influenced by mixed convection and considered to be in the forced convection regime.

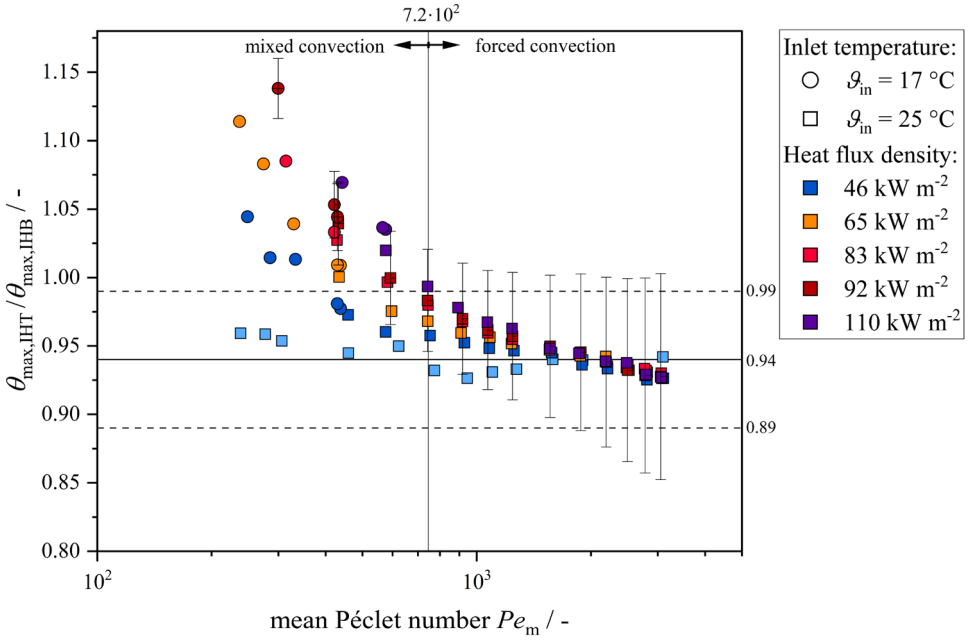

Fig. 10. Quotient of maximum dimensionless temperature for IHT and IHB $\theta_{max,IHT}/\theta_{max,IHB}$ versus mean Péclet number Pe_m at different heat flux densities. The exemplary uncertainty of measurement for $\dot{q}_w = 92$ kW m^{-2} is shown.

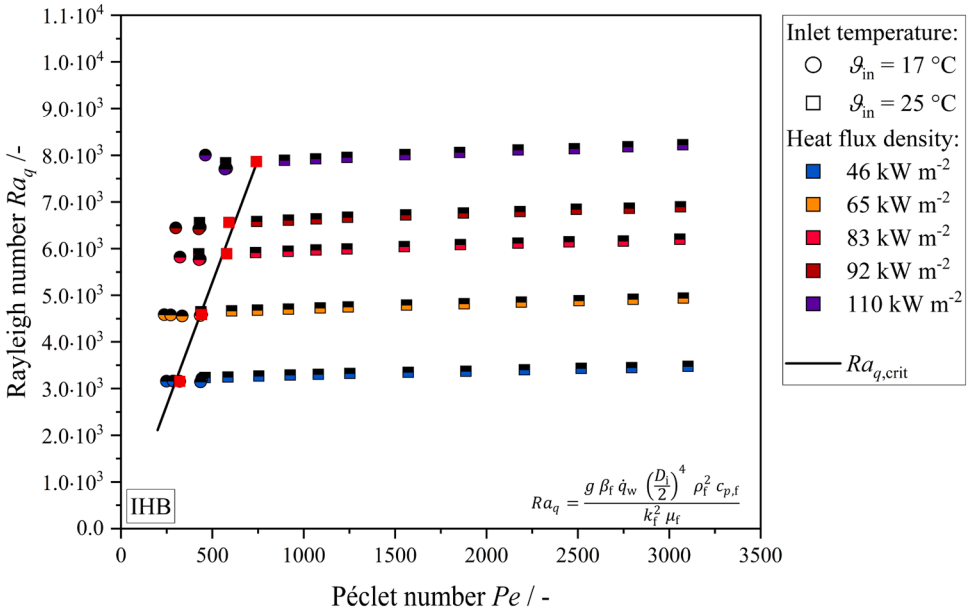

Fig. 11. Rayleigh number Ra_q versus Péclet number Pe for IHB. The data points and their uncertainty of measurement for which mixed convection occurs first with decreasing Pe based on $\theta_{max,IHT}/\theta_{max,IHB} > 0.99$ are marked with red squares.

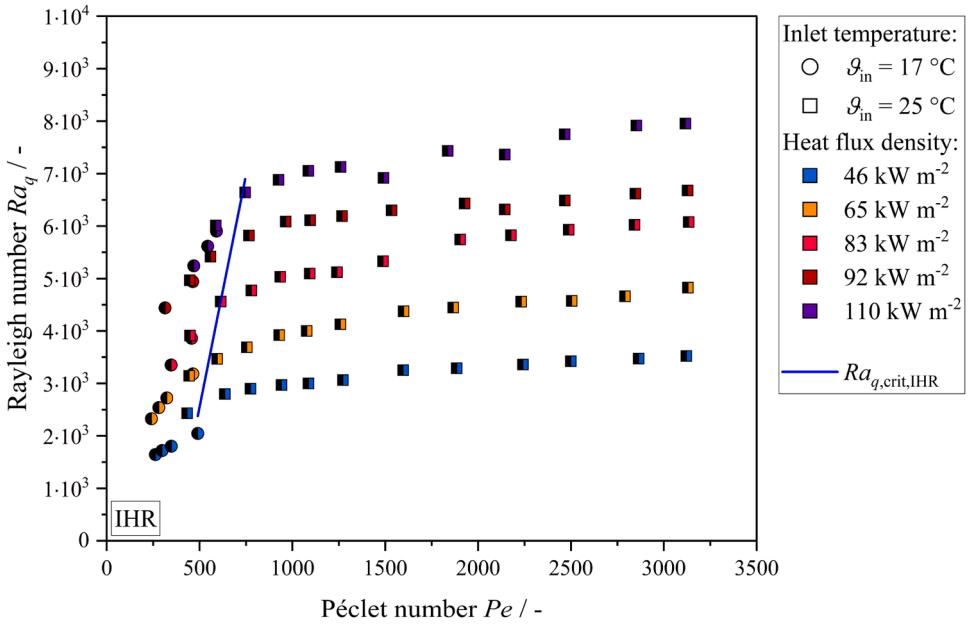

Fig. 12. Rayleigh number Ra_q versus Péclet number Pe for IHR.

The correlation for the critical Rayleigh number is derived from the data illustrated in Fig. 11 and is defined as stated in Eq. (20).

$$Ra_{q,crit,IHB} = 10.552\ Pe \tag{20}$$

It is valid for $300 < Pe < 750$, presenting an expansion of the Rayleigh correlation of Laube [17]. Eq. (20) was derived by fitting a linear equation to the data points that satisfy the criterion $\theta_{max,IHT}/\theta_{max,IHB} > 0.99$.

For IHR and IHBR, a different behavior of Ra_q is observed. Contrary to IHB, a change of slope is visible in Fig. 12 for IHR and IHBR which supports the assumption of different flow patterns caused by buoyancy effects depending on the orientation of the heat flux. At high Pe, Ra_q reaches almost constant values, indicating that pure forced convection is present. With decreasing Pe, a pronounced decrease of Ra_q for all heat flux densities is visible and a new correlation is calculated according to Eq. (21).

$$Ra_{q,crit,IHR} = 17.682\ Pe - 6290.357 \tag{21}$$

For $Ra_q > Ra_{q,crit,IHR}$ mixed convection is assumed. Similar curves exist for IHBR, but they show a less pronounced change of slope at low Pe. The correlation of $Ra_{q,crit,IHR}$ can be applied to the data of IHBR (see Fig. 22 in Appendix D) with sufficient accuracy.

4.3.2. Buhr parameter

Further, the Buhr parameter Z is applied to the data and mixed convection is determined based on $\theta_{max,IHT}/\theta_{max,IHB} > 0.99$. Fig. 13

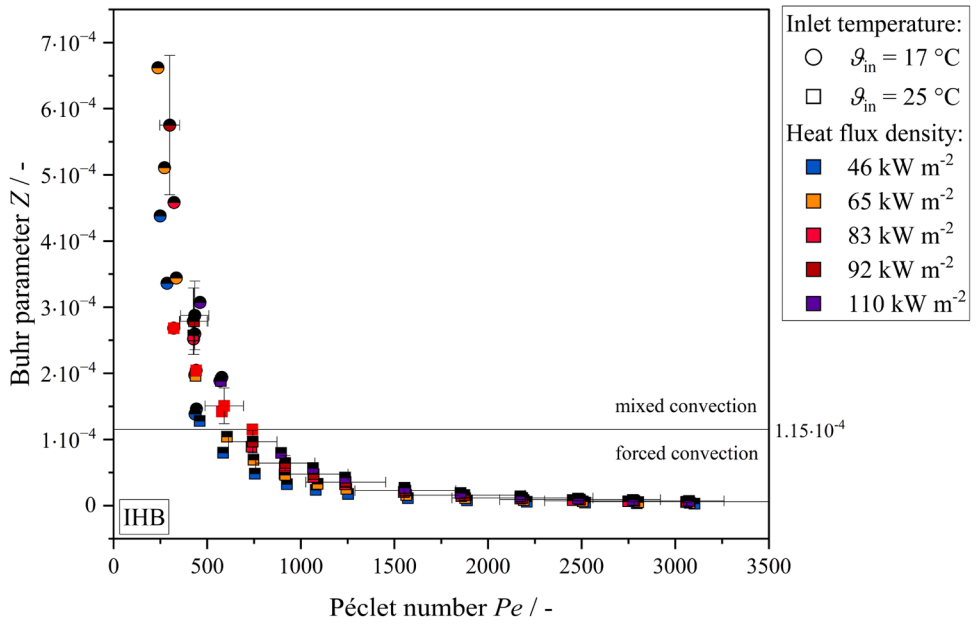

Fig. 13. Buhr parameter Z versus Péclet number Pe for IHB at different heat flux densities. The data points for which mixed convection occurs first with decreasing Pe based on $\theta_{max,IHT}/\theta_{max,IHB} > 0.99$ are marked with red squares. The exemplary uncertainty of measurement for $\dot{q}_w = 92$ kW m^{-2} is shown.

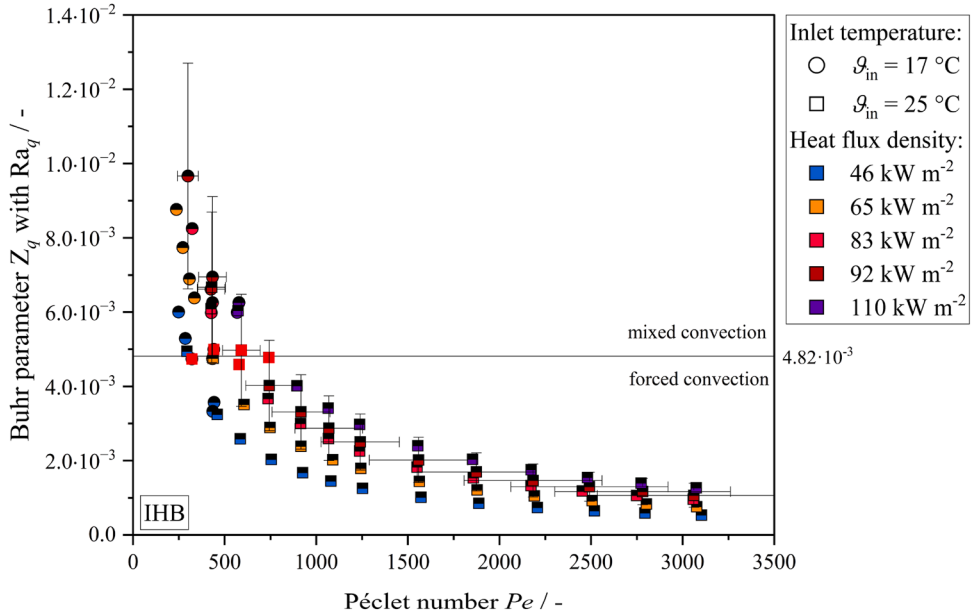

Fig. 14. Buhr parameter Z_q versus Péclet number Pe for IHB. The data points for which mixed convection occurs first with decreasing Pe based on $\theta_{max,IHT}/\theta_{max,IHB} > 0.99$ are marked with red squares. The exemplary uncertainty of measurement for $\dot{q}_w = 92$ kW m^{-2} is shown.

shows the Buhr parameter for IHB calculated with Eq. (4) and the axial temperature difference defined in Eq. (5). Here, the original definition of Buhr et al. [26] for vertical tubes is applied to the present data from a horizontal tube.

For increasing Pe, Z reaches a threshold for all heat flux densities. For $Pe < 1 \times 10^3$, Z increases with decreasing Pe and shows a dependency on the heat flux density, indicating the occurrence of mixed convection. The evaluation of mixed convection based on $\theta_{max,IHT}/\theta_{max,IHB} > 0.99$ shows that, contrary to the statement by Buhr et al. [26] mixed convection already occurs for $Z_{crit} > 1.15 \times 10^{-4}$. This limit falls below the specified criterion of $Z > 2 \times 10^{-3}$ given by Buhr et al. [26] by an order of magnitude, which was questioned before [27]. This means that for a heated liquid metal flow in a horizontal tube, mixed convective effects already occur at a higher flowrate or at lower heat fluxes than predicted. The work of Gardner and Lykoudis [27] supports the findings of the present work. They conducted experiments with a mercury flow in a horizontal tube with inhomogeneous heat flux and observed the distortion of temperature profiles due to buoyancy effects for $Z > 1.2 \times 10^{-3}$. This indicates that mixed convection in horizontal liquid metal flows is present for smaller Z than predicted by Buhr et al. [26] for a vertical flow.

Since the occurrence of mixed convection for IHR and IHBR is evaluated based on the change of slope of the Rayleigh number Ra_q which is calculated with the heat flux density, the original definition of

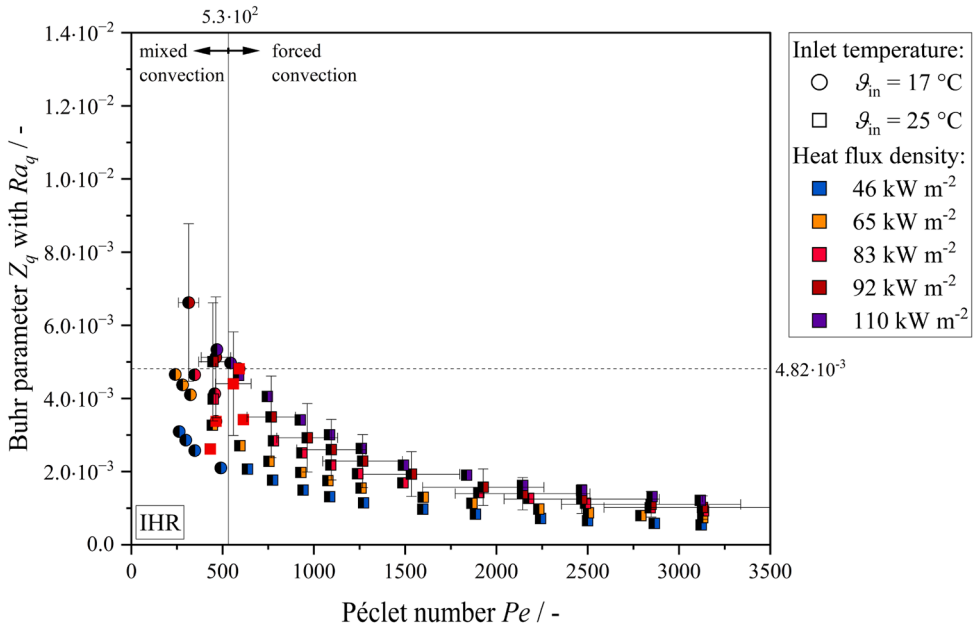

Fig. 15. Buhr parameter Z_q versus Péclet number Pe for IHR. The data points for which mixed convection occurs first with decreasing Pe based on $Ra_{q,crit,IHR}$ are marked with red squares. The exemplary uncertainty of measurement for $\dot{q}_w$ = 92 kW m^{-2} is shown.

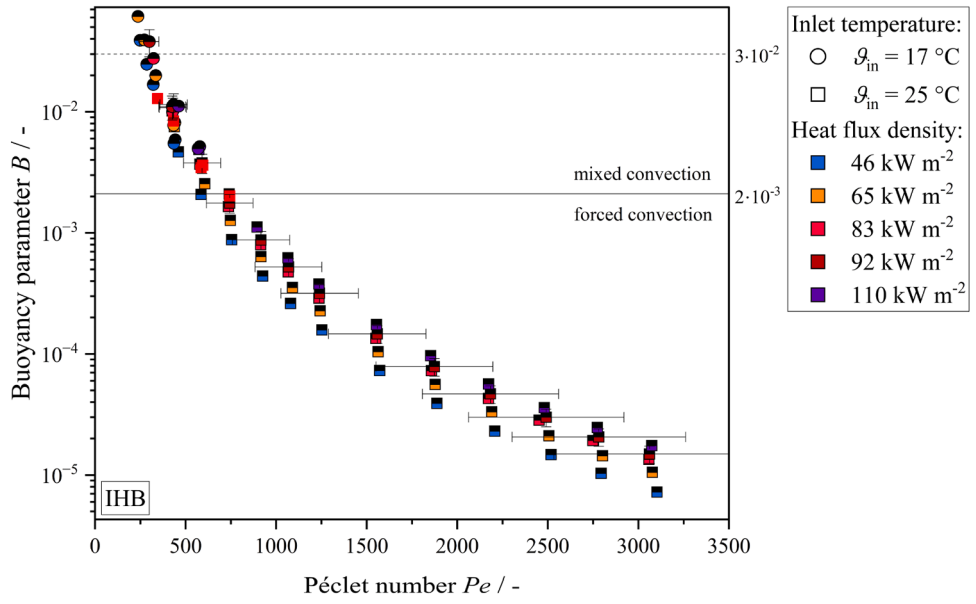

Fig. 16. Buoyancy parameter B versus Péclet number Pe for IHB at different heat fluxes. The data points for which mixed convection occurs first with decreasing Pe based on $\theta_{max,IHT}/\theta_{max,IHB} > 0.99$ are marked with red squares. The exemplary uncertainty of measurement for $\dot{q}_w$ = 92 kW m^{-2} is shown.

the Buhr parameter is adapted. Calculating the Buhr parameter with the temperature gradient parallel to the direction of gravitation instead of the temperature difference between the outlet and inlet of the horizontal tube leads to the expression given in Eq. (22).

$$Z_q = \frac{g\ \beta\ \overline{\dot{q}_{wi}} \left(\frac{D_i}{2}\right)^4 \rho^2\ c_p\ \pi\ D_i^2}{4\ k^2\ \dot{M}\ L} \tag{22}$$

Herein, $\overline{\dot{q}_{wi}}$ is the mean heat flux density on the inside of the tube. Applying this definition to the data leads to figure Fig. 14, showing Z_q for IHB.

The evaluation of mixed convection based on $\theta_{max,IHT}/\theta_{max,IHB} > 0.99$ reveals that the values of Z_q under mixed convection exceed $Z_{q,crit} = 4.82 \times 10^{-3}$. No dependency of $Z_{q,crit}$ on the heat flux density is visible. Therefore, this threshold is determined by averaging the values of Z_q for which mixed convection occurs. Contrary, Fig. 15 shows a dependency of $Z_{q,crit}$ on the heat flux density for IHR.

Applying the limit derived from IHB to the data of IHR reveals, that only a few data points are located in the region of mixed convection. As with the Rayleigh number, the criterion determined with IHB cannot be applied to the data from IHR, which supports the theory of different flow patterns caused by buoyancy depending on the direction of heat flux. Instead, the averaged limits of Z_q for the data points that are located in the mixed convection regime based on $Ra_{q,crit,IHR}$ result in $Pe_{crit} < 5.3 \times 10^2$. The same value results from the data for IHBR (see Fig. 23 in Appendix D). I.e., in contrast to the data for IHB, no critical Buhr parameter

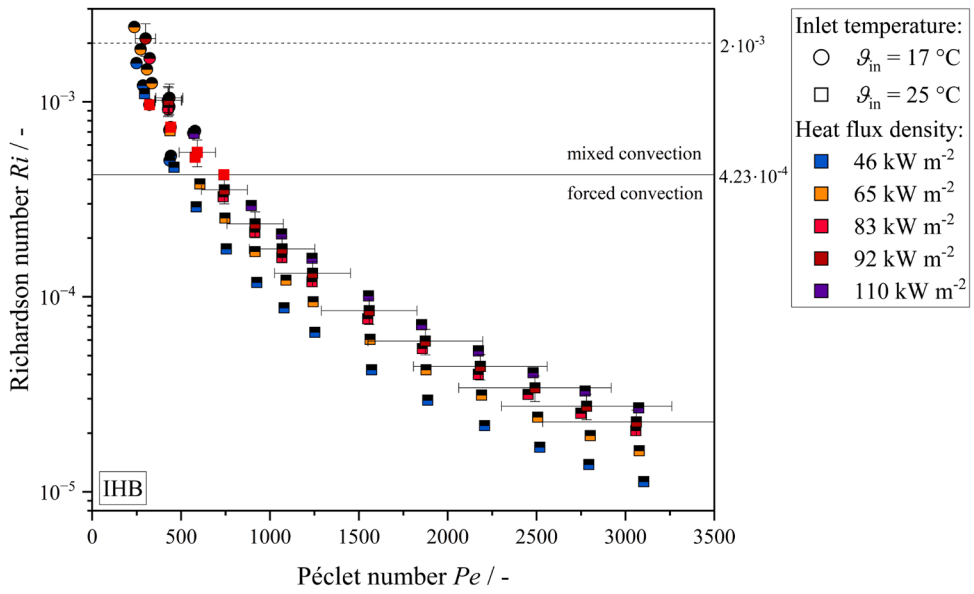

Fig. 17. Richardson number *Ri* versus Péclet number *Pe* for different heat flux densities for IHB. The data points for which mixed convection occurs first with decreasing *Pe* based on $\theta_{max,IHT}/\theta_{max,IHB} > 0.99$ are marked with red squares. The exemplary uncertainty of measurement for $\dot{q}_w = 92$ kW m^{-2} is shown.

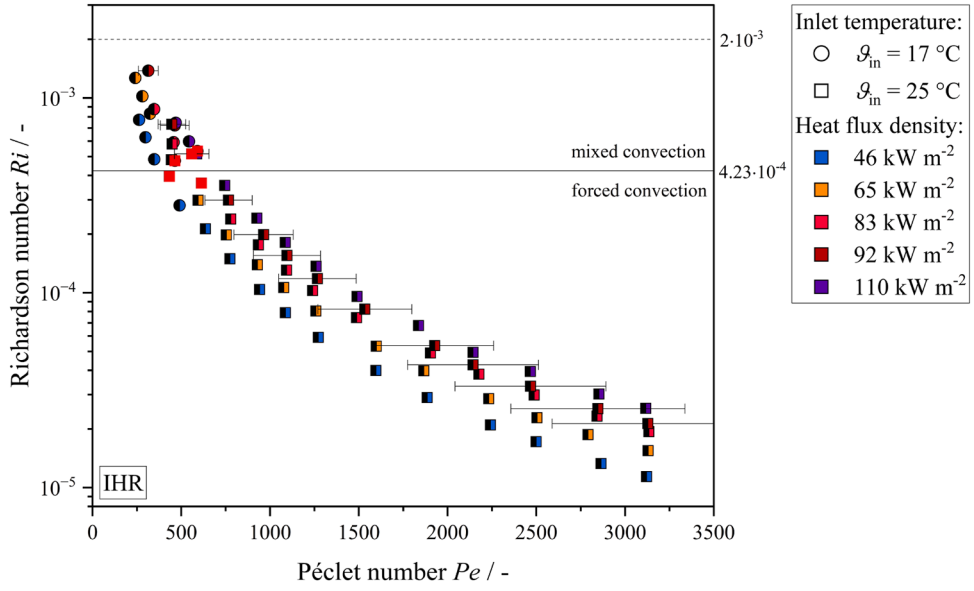

Fig. 18. Richardson number *Ri* versus Péclet number *Pe* for different heat flux densities for IHR. The data points for which mixed convection occurs first with decreasing *Pe* based on $Ra_{q,crit,IHR}$ are marked with red squares. The exemplary uncertainty of measurement for $\dot{q}_w = 92$ kW m^{-2} is shown.

can be derived from the existing data for IHR, only a limit for the Péclet number.

4.3.3. Buoyancy parameter

The third parameter used in literature to quantify mixed convection in liquid metal flows is the Buoyancy parameter, defined in Eq. (6).

As shown in Fig. 16, only four data points present a Buoyancy parameter of $B > 3 \times 10^{-2}$ and are located in the mixed convection regime according to Celata et al. [30]. Contrary to this, the quotient of θ_{max} shows that mixed convection affects the heat transfer for $B > 2 \times 10^{-3}$. No change in the curves is recognizable and based on *B* it is not possible to differentiate between mixed and forced convection in the present data set. That is not surprising though, as the Buoyancy parameter is based on the thermal boundary layer thickness of ordinary fluids and therefore, its use for the liquid metal flows addressed in this work indeed seems inappropriate. Consequently, the regime limit derived from fluids with $Pr \geq 0.7$ cannot be applied to liquid metals.

4.3.4. Richardson number

The fourth parameter mentioned in the present work as a potential criterion is the Richardson number, which is defined as stated in the nomenclature section. As shown in Fig. 17, *Ri* is decreasing with

increasing *Pe*, presenting a similar course as the buoyancy parameter *B* and the Buhr parameter *Z*.

The threshold of $Ri > 0.3$ for mixed convection is clearly out of data range and not applicable to liquid metals, since it was theoretically conducted for ordinary fluids by Sparrow et al. [25]. The threshold of $Ri > 2 \times 10^{-3}$ from Jackson et al. [19], derived from a vertical sodium flow, does not coincide with the mixed convection criterion based on $\theta_{\mathrm{max,IHT}}/\theta_{\mathrm{max,IHB}} > 0.99$, although it is in the range of our data. Therefore, we derive a new limit from the present data, resulting in $Ri_{q,\mathrm{crit}} = 4.23 \times 10^{-4}$. This value corresponds to the mean value of the limit values of *Ri*, which are determined using $Ra_{q,\mathrm{crit,IHB}}$. The same value results from the data of IHR (see Fig. 18) and IHBR (see Fig. 24 in Appendix D).

Heat transfer data available in the literature on heat transfer in liquid metal tube flows predominantly addresses cases with uniform heating conditions [9,19]. Only a limited number of studies generally explore the regime of mixed convection in a horizontal tube [23,27,48]. However, these contributions do not disclose enough information on the experimental setup and flow characteristics to calculate the Richardson number or other mixed convection criteria considered in this work. As a result, a direct comparison of the experimental results presented here and existing literature data is not feasible.

5. Conclusions

This study investigated the heat transfer characteristics of a horizontal liquid metal tube flow under inhomogeneous heating conditions and the onset of mixed convection. Four different directions of heating have been examined. The results confirm that the azimuthally averaged Nusselt number $\langle Nu \rangle$ increases with the Péclet number *Pe* and shows no dependency on the heat flux distribution. However, the azimuthal distribution of the dimensionless temperature θ varies with the heat flux density for low Péclet numbers depending on the direction of heating, indicating an influence of buoyancy effects on flow pattern of the liquid metal. This is particularly observed for heating directions non-parallel to the direction of gravitational acceleration. Various criteria for the onset of mixed convection were discussed and applied to the available data. Using the critical Rayleigh number $Ra_{q,\mathrm{crit}}$ (see Eq. (23)) and the Buhr parameter Z_q as parameters for the characterization of the onset of mixed convection in liquid metals is recommended.

$$Ra_{q,\mathrm{crit}} = \begin{cases} 10.552\ Pe, & \text{IHB} \\ 17.682\ Pe - 6290.357, & \text{IHR and IHBR} \end{cases} \tag{23}$$

Despite its original formulation for vertical flow configurations, the Buhr parameter has proven to be relevant for the horizontal mixed convection considered in this study. Traditional parameters like the Buoyancy parameter have been assessed and deemed unsuitable for the application on low-Prandtl number fluids, especially when determined by experimental data or theoretical derivations for ordinary fluids. These findings are relevant for the thermal design of liquid metal systems with strongly non-uniform heat flux distributions, since the accurate prediction of local wall temperatures and wall stresses are essential for the life time prediction of pipes and tubes. A detailed differentiation between buoyancy-induced flow modifications and effects arising from temperature-dependent material properties, such as viscosity variations of liquid metals, was beyond the scope of this study. Future work, including CFD investigations and velocity-profile measurements in an upcoming experimental configuration, will help to clarify their respective impact on heat-transfer behavior.

A database of the experimental data of the results presented here is available in the open-access repository KITopen [49].

CRediT authorship contribution statement

Linda Elmlinger: Writing – review & editing, Writing – original draft, Visualization, Validation, Software, Methodology, Investigation, Formal analysis, Data curation, Conceptualization. **Tim Laube:** Validation, Software, Methodology, Conceptualization. **Benjamin Dietrich:** Writing – review & editing, Supervision, Project administration, Funding acquisition. **Thomas Wetzel:** Writing – review & editing, Supervision, Project administration, Funding acquisition.

Declaration of competing interest

The authors declare that they have no known competing financial interests or personal relationships that could have appeared to influence the work reported in this paper.

Acknowledgments

The authors would like to thank the German Research Foundation (DFG) for funding the research project WE 4672/42. Additionally, the authors would like to thank Lennart Winter and the team of the KArlsruhe Liquid metal LAboratory (KALLA) for supporting this work.

Appendix A

Physical properties of nickel Alloy 201

Table 4
Physical properties of Alloy 201, taken from [17].

Physical property	Correlation	Uncertainty
Density	$\rho_{\mathrm{Alloy201}}(T = 297.15\ \mathrm{K}) = 8484.1\ \mathrm{kg\ m^{-3}}$	± 0.55 %
Specific heat capacity at constant pressure, $p = 1$ bar	$\frac{c_{p,\mathrm{Alloy201}}(T)}{\mathrm{J\ kg^{-1}\ K^{-1}}} = 0.502\ \frac{T}{\mathrm{K}} + 287.154$	± 3.1 %
Temperature conductivity	$\frac{\kappa_{\mathrm{Alloy201}}(T)}{\mathrm{m^2\ s^{-1}}} = -3.754 \times 10^{-8}\ \frac{T}{\mathrm{K}} + 3.15 \times 10^{-5}$	± 1.4 %
Thermal conductivity	$\frac{k_{\mathrm{Alloy201}}(T)}{\mathrm{W\ m^{-1}\ K}} = -0.065\ \frac{T}{\mathrm{K}} + 94.651$	± 3.3 %

Appendix B

Aging of the test tube

To rule out effects of aging of the test section due to corrosion and the build-up of an oxide layer, measurements with a time gap of one year are compared. As show in Fig. 19, the data is within the range of the measurement uncertainty of the reference data. Additional data varying the direction of heating and heat flux confirm that there have been no changes of the test tube after one year.

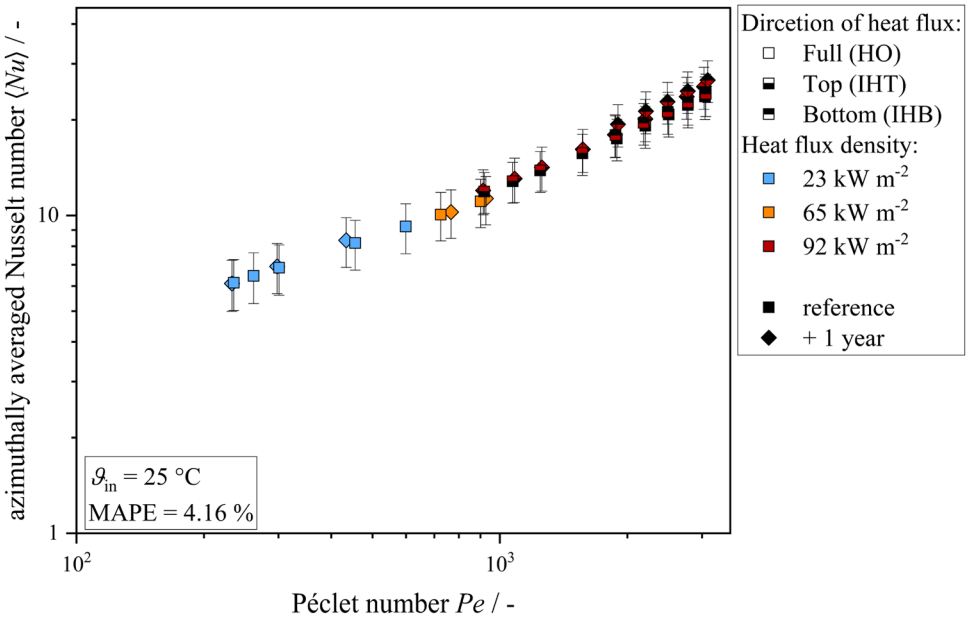

Fig. 19. Comparison of measurements under different heating and flow conditions with identical measurements one year apart.

Appendix C

Nusselt correlations

New correlations of the obtained data depending on the direction of heat flux result in following correlations with a coefficient of determination $R^2 > 0.98$:

$$\langle Nu \rangle = 4.364 + 0.0276\ Pe^{0.801} \text{ for HO [17]} \tag{24}$$

$$\langle Nu \rangle = 4.364 + 0.0315\ Pe^{0.801} \text{ for IHT} \tag{25}$$

$$\langle Nu \rangle = 4.364 + 0.059\ Pe^{0.723} \text{ for IHB} \tag{26}$$

$$\langle Nu \rangle = 1.154 + 0.0495\ Pe^{0.761} \text{ for IHR} \tag{27}$$

$$\langle Nu \rangle = 1.168 + 0.0482\ Pe^{0.771} \text{ for IHBR} \tag{28}$$

The correlations are valid for $2.4 \times 10^2 < Pe < 3.1 \times 10^3$.

Appendix D

Additional information on dimensionless temperature

In order to present all information discussed in section 4.2, additional figures on θ_{max} and θ_{min} are presented.

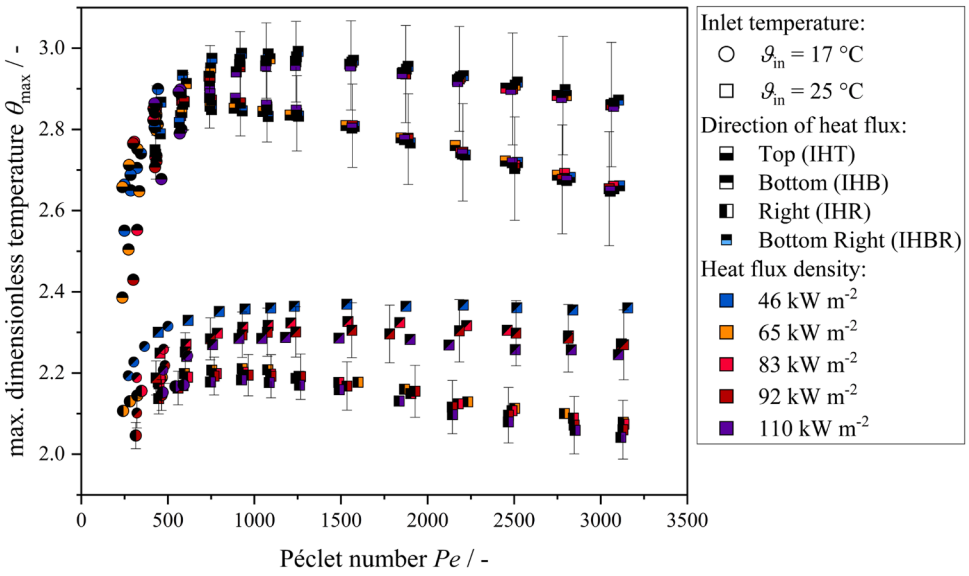

Fig. 20. Comparison of maximum of dimensionless temperature θ_{max} versus Péclet number Pe for different heating conditions and heat flux densities. The exemplary uncertainty of measurement for $\dot{q}_w = 92$ kW m^{-2} is shown.

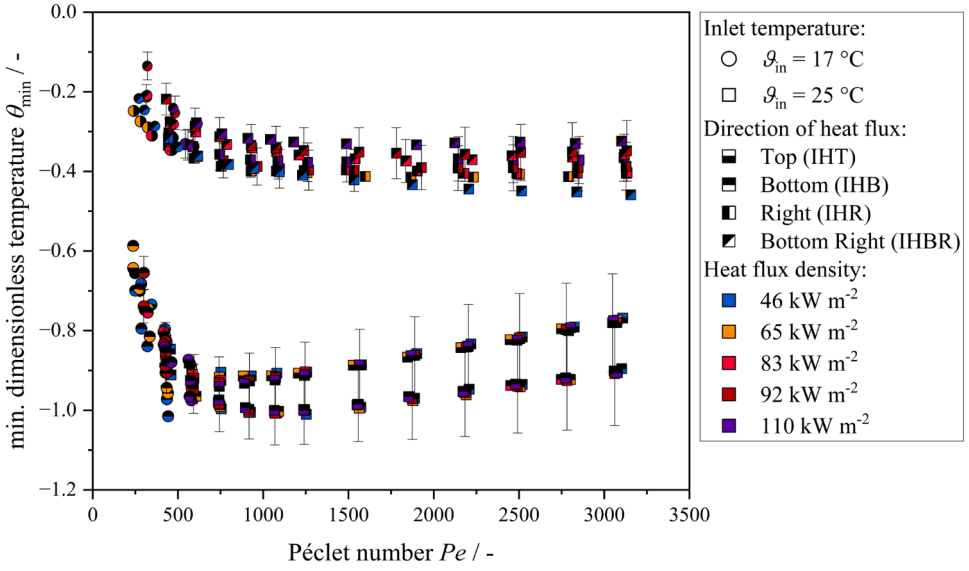

Fig. 21. Comparison of minimum of dimensionless temperature θ_{min} versus Péclet number Pe for different heating conditions and heat flux densities. The exemplary uncertainty of measurement for $\dot{q}_w = 92$ kW m^{-2} is shown.

Additional information on IHBR

In order to present all information discussed in section 4.3, additional figures on IHBR are presented.

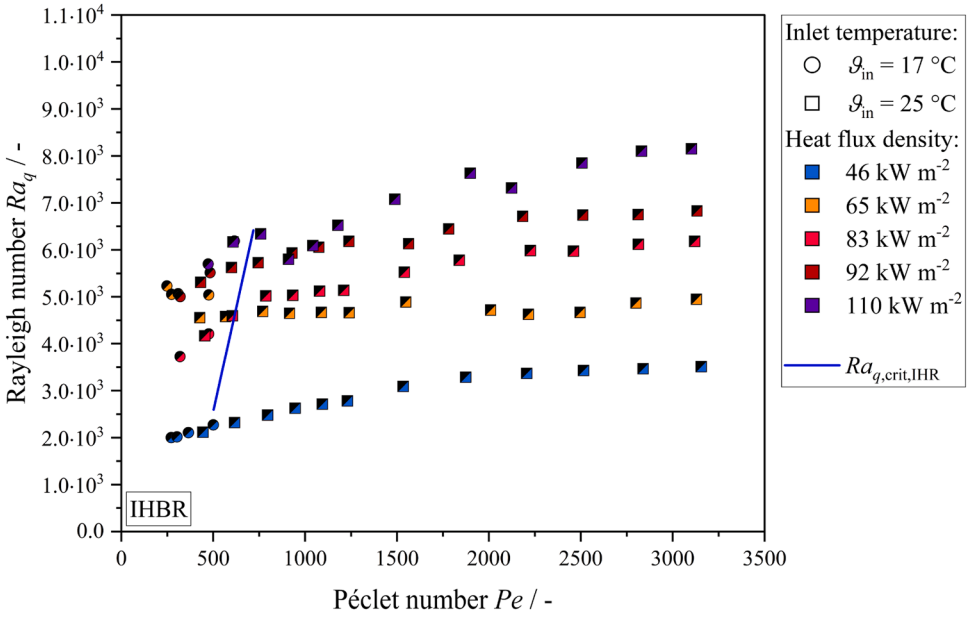

Fig. 22. Rayleigh number Ra_q versus Péclet number Pe for IHBR.

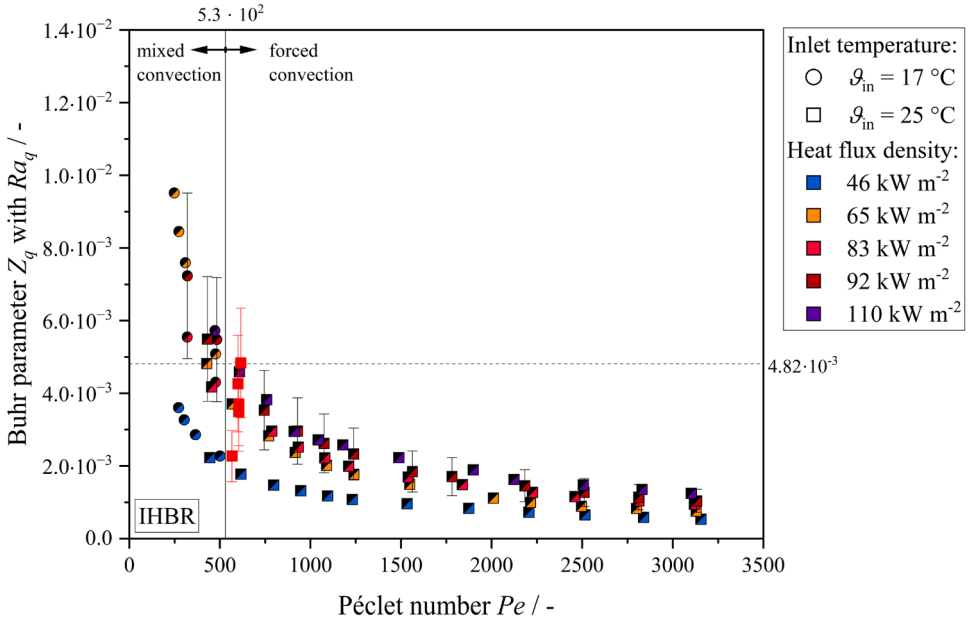

Fig. 23. Buhr parameter Z_q versus Péclet number Pe for IHBR. The data points for which mixed convection occurs first with decreasing Pe based on $Ra_{q,crit,IHR}$ are marked with red squares. The exemplary uncertainty of measurement for $\dot{q}_w$ = 92 kW m^{-2} is shown.

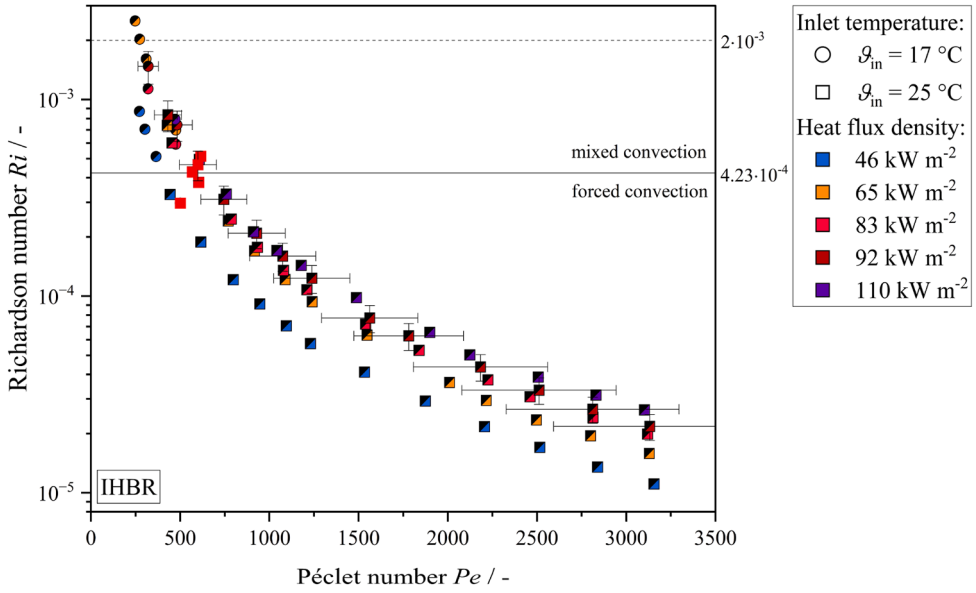

Fig. 24. Richardson number *Ri* versus Péclet number *Pe* for different heat flux densities for IHBR. The data points for which mixed convection occurs first with decreasing *Pe* based on $Ra_{q,\mathrm{crit,IHR}}$ are marked with red squares. The exemplary uncertainty of measurement for $\dot{q}_w = 92$ kW m^{-2} is shown.

References

[1] A. Fritsch, J. Flesch, V. Geza, C. Singer, R. Uhlig, B. Hoffschmidt, Conceptual study of Central receiver systems with liquid metals as efficient heat transfer fluids, Energy Procedia 69 (2015) 644–653, https://doi.org/10.1016/j.egypro.2015.03.074.

[2] A. Heinzel, et al., Liquid metals as efficient high-temperature heat-transport fluids, Energy Technol. 5 (7) (2017) 1026–1036, https://doi.org/10.1002/ente.201600721.

[3] K. Niedermeier, A perspective on high-temperature heat storage using liquid metal as heat transfer fluid, Energy Storage 5 (8) (Dec. 2023) e530, https://doi.org/10.1002/est2.530.

[4] X. Cheng, N. Tak, Investigation on turbulent heat transfer to lead–bismuth eutectic flows in circular tubes for nuclear applications, Nucl. Eng. Des. 236 (4) (2006) 385–393, https://doi.org/10.1016/j.nucengdes.2005.09.006.

[5] I.A. Belyaev, et al., Test facility for investigation of heat transfer of promising coolants for the nuclear power industry, Therm. Eng. 64 (11) (2017) 841–848, https://doi.org/10.1134/S0040601517110027.

[6] G. Bo, L. Ren, X. Xu, Y. Du, S. Dou, Recent progress on liquid metals and their applications, Adv. Phys. X 3 (1) (2018) 1446359, https://doi.org/10.1080/23746149.2018.1446359.

[7] J. Pacio, C. Singer, Th. Wetzel, R. Uhlig, Thermodynamic evaluation of liquid metals as heat transfer fluids in concentrated solar power plants, Appl. Therm. Eng. 60 (1–2) (2013) 295–302, https://doi.org/10.1016/j.applthermaleng.2013.07.010.

[8] L. Marocco, G. Cammi, J. Flesch, Th. Wetzel, Numerical analysis of a solar tower receiver tube operated with liquid metals, Int. J. Therm. Sci. 105 (2016) 22–35, https://doi.org/10.1016/j.ijthermalsci.2016.02.002.

[9] H.O. Buhr, A. Sesonske, Temperature distributions in liquid metals for turbulent flow in a horizontal pipe with free convection, Nucl. Eng. Des. 31 (1) (1974) 46–56, https://doi.org/10.1016/0029-5493(74)90132-0.

[10] C. Marugán-Cruz, O. Flores, D. Santana, M. García-Villalba, Heat transfer and thermal stresses in a circular tube with a non-uniform heat flux, Int. J. Heat Mass Transf. 96 (2016) 256–266, https://doi.org/10.1016/j.ijheatmasstransfer.2016.01.035.

[11] W.R. Logie, J.D. Pye, J. Coventry, Thermoelastic stress in concentrating solar receiver tubes: A retrospect on stress analysis methodology, and comparison of salt and sodium, Sol. Energy 160 (2018) 368–379, https://doi.org/10.1016/j.solener.2017.12.003.

[12] J.K. Jacoby, A. Sesonske, Free convection distortion and eddy diffusivity effects in turbulent mercury heat transfer, Trans. Am. Nucl. Soc. 15 (1) (1972) 408–409.

[13] OECD and Nuclear Energy Agency, Handbook On Lead-Bismuth Eutectic Alloy and Lead Properties, Materials Compatibility, Thermalhydraulics and Technologies, Nuclear Science Publishing, 2015, https://doi.org/10.1787/42dcd531-en.

[14] W. Jaeger, Empirical models for liquid metal heat transfer in the entrance region of tubes and rod bundles, Heat. Mass Transf. 53 (5) (2017) 1667–1684, https://doi.org/10.1007/s00231-016-1929-8.

[15] O. Zikanov, I. Belyaev, Y. Listratov, P. Frick, N. Razuvanov, V. Sviridov, Mixed convection in pipe and duct flows with strong magnetic fields, Appl. Mech. Rev. 73 (1) (2021), https://doi.org/10.1115/1.4049833, 010801 vols.

[16] T. Laube, B. Dietrich, L. Marocco, T. Wetzel, Conjugate heat transfer of a turbulent tube flow of water and GaInSn with azimuthally inhomogeneous heat flux, Int. J. Heat Mass Transf. 221 (2024), https://doi.org/10.1016/j.ijheatmasstransfer.2023.125027.

[17] T. Laube, Wärmeübergang in turbulenten Flüssigmetallrohrströmungen mit azimutal inhomogener verteilung der Wärmestromdichte, Karlsruher Institut für Technologie (KIT) (2024) [Online]. Available: https://publikationen.bibliothek.kit.edu/1000171445.

[18] W. Jäger, W. Hering, Mixed convection with liquid metals: review of experiments and model development. presented At the Advances in Thermal Hydraulics (ATH 2018), 2018, https://doi.org/10.5445/IR/1000087243.

[19] J.D. Jackson, Turbulent mixed convection heat transfer to liquid sodium, Int. J. Heat Fluid Flow 4 (2) (1983) 107–111, https://doi.org/10.1016/0142-727X(83)90011-5.

[20] W. Guo, A. Shams, Y. Sato, B. Niceno, Influence of buoyancy in a mixed convection liquid metal flow for a horizontal channel configuration, Int. J. Heat Fluid Flow 85 (2020) 108630, https://doi.org/10.1016/j.ijheatfluidflow.2020.108630.

[21] H.O. Buhr, E.A. Horsten, A.D. Carr, The distortion of turbulent velocity and temperature profiles on heating, for mercury in a vertical pipe, J. Heat Transf. 96 (2) (1974) 152–158, https://doi.org/10.1115/1.3450156.

[22] S. Moolya, A. Satheesh, Role of magnetic field and cavity inclination on double diffusive mixed convection in rectangular enclosed domain, Int. Commun. Heat Mass Transf. 118 (2020) 104814, https://doi.org/10.1016/j.icheatmasstransfer.2020.104814.

[23] M. Wang, T. Tsuji, Y. Nagano, Mixed convection with flow reversal in the thermal entrance region of horizontal and vertical pipes, Int. J. Heat Mass Transf. 37 (15) (1994) 2305–2319, https://doi.org/10.1016/0017-9310(94)90372-7.

[24] B. Metais, E.R.G. Eckert, Forced, mixed, and free convection regimes, J. Heat Transf. 86 (2) (1964) 295–296, https://doi.org/10.1115/1.3687128.

[25] E.M. Sparrow, R. Eichhorn, J.L. Gregg, Combined forced and free convection in a boundary layer flow, Phys. Fluids 2 (3) (1959) 319–328, https://doi.org/10.1063/1.1705928.

[26] H.O. Buhr, A.D. Carr, R.E. Balzhiser, Temperature profiles in liquid metals and the effect of superimposed free convection in turbulent flow, Int. J. Heat Mass Transf. 11 (4) (1968) 641–654, https://doi.org/10.1016/0017-9310(68)90067-7.

[27] R.A. Gardner, P.S. Lykoudis, Magneto-fluid-mechanic pipe flow in a transverse magnetic field with and without heat transfer, in: AIAA Fluid and Plasma Dynamics Conference, AIAA PAper, 1969.

[28] W.B. Hall, J.D. Jackson, Laminarization of a turbulent pipe flow by buoyancy forces, ASME Pap. (1969), 69-HT-55.

[29] J.D. Jackson, M.A. Cotton, B.P. Axcell, Studies of mixed convection in vertical tubes, Int. J. Heat Fluid Flow 10 (1) (1989) 2–15, https://doi.org/10.1016/0142-727X(89)90049-0.

[30] G.P. Celata, F. D'Annibale, A. Chiaradia, M. Cumo, Upflow turbulent mixed convection heat transfer in vertical pipes, Int. J. Heat Mass Transf. 41 (24) (1998) 4037–4054, https://doi.org/10.1016/S0017-9310(98)00177-X.

[31] T.L. Bergman, A.S. Lavine, Fundamentals of Heat and Mass Transfer, Eighth edition, John Wiley & Sons, Hoboken, NJ, 2017.

[32] T. Laube, F. Emmendörfer, B. Dietrich, L. Marocco, T. Wetzel, Thermophysical Properties of the Near Eutectic Liquid Ga-In-Sn Alloy, Karlsruhe Institute of Technology, 2023, https://doi.org/10.35097/1548.

[33] P. Geddis, L. Wu, A. McDonald, S. Chen, B. Clements, Effect of static liquid Galinstan on common metals and non-metals at temperatures up to 200°C, Can. J. Chem. 98 (12) (2020) 787–798, https://doi.org/10.1139/cjc-2020-0227.
[34] V. Ya. Prokhorenko, V.V. Roshchupkin, M.A. Pokrasin, S.V. Prokhorenko, V. V. Kotov, Liquid gallium: potential uses as a heat-transfer agent, High Temp. 38 (6) (2000) 954–968, https://doi.org/10.1023/A:1004157827093.
[35] Y. Plevachuk, V. Sklyarchuk, S. Eckert, G. Gerbeth, R. Novakovic, Thermophysical properties of the liquid Ga–In–Sn eutectic alloy, J. Chem. Eng. Data 59 (3) (2014) 757–763, https://doi.org/10.1021/je400882q.
[36] L. Barleon, K.J. Mack, and R. Stieglitz, "The MEKKA-facility a flexible tool to investigate MHD flow phenomena," Karlsruhe, 1996. doi: 10.5445/IR/270039825.
[37] Y.-L. He, W. Wang, R. Jiang, M. Li, W. Tao, Liquid-based high-temperature receiver technologies for next-generation concentrating solar power: A review of challenges and potential solutions, Front. Energy 17 (1) (2023) 16–42, https://doi.org/10.1007/s11708-023-0866-8.
[38] International Organization for Standardization, Guide to the Expression of Uncertainty in Measurement (GUM:1995), 2008. Guide 98–3.
[39] V. Gnielinski, Neue gleichungen für den Wärme- und den Stoffübergang in turbulent durchströmten Rohren und Kanälen, Forsch. Im Ingenieurwesen 41 (1) (1975) 8–16, https://doi.org/10.1007/BF02559682.
[40] R.R. Schmidt, E.M. Sparrow, Turbulent flow of water in a tube with circumferentially nonuniform heating, with or without buoyancy, J. Heat Transf. 100 (3) (1978) 403–409, https://doi.org/10.1115/1.3450822.
[41] T. Laube, B. Dietrich, L. Marocco, T. Wetzel, Turbulent heat transfer in a liquid metal tube flow with azimuthally inhomogeneous heat flux, Int. J. Heat Mass Transf. 189 (2022) 122734, https://doi.org/10.1016/j.ijheatmasstransfer.2022.122734.
[42] C.-J. Chen, J.S. Chiou, Laminar and turbulent heat transfer in the pipe entrance region for liquid metals, Int. J. Heat Mass Transf. 24 (7) (1981) 1179–1189, https://doi.org/10.1016/0017-9310(81)90167-8.
[43] T. Laube, B. Dietrich, L. Marocco, T. Wetzel, Heat Transfer and Pressure Drop Data of a Turbulent Tube Flow of Water and GaInSn with Azimuthally Inhomogeneous Heat Flux, Karlsruher Institut für Technologie (KIT), 2023, https://doi.org/10.5445/IR/1000155030.
[44] I.F. Okafor, J. Dirker, J.P. Meyer, Influence of circumferential solar heat flux distribution on the heat transfer coefficients of linear Fresnel collector absorber tubes, Sol. Energy 107 (2014) 381–397, https://doi.org/10.1016/j.solener.2014.05.011.
[45] W.A. Sutherland, W.M. Kays, Heat transfer in an annulus with variable circumferential heat flux, Int. J. Heat Mass Transf. 7 (11) (Nov. 1964) 1187–1194, https://doi.org/10.1016/0017-9310(64)90060-2.
[46] J. Flesch, "LBE-cooled tube receiver performance - design aspects and high-flux operation in a solar furnace," 2021, 10.5445/IR/1000128683.
[47] Y. Xu, R. Tian, X. Dai, L. Shi, Coupling effect between heat flux distribution and buoyancy of supercritical CO2 heat transfer with nonuniform heat flux in parabolic-trough collector, Int. J. Heat Mass Transf. 195 (2022) 123197, https://doi.org/10.1016/j.ijheatmasstransfer.2022.123197.
[48] S. Straub, P. Forooghi, L. Marocco, T. Wetzel, B. Frohnapfel, Azimuthally inhomogeneous thermal boundary conditions in turbulent forced convection pipe flow for low to medium prandtl numbers, Int. J. Heat Fluid Flow 77 (2019) 352–358, https://doi.org/10.1016/j.ijheatfluidflow.2019.05.003.
[49] L. Elmlinger, B. Dietrich, T. Wetzel, Heat Transfer Data of a Horizontal Turbulent Tube Flow of GaInSn with Azimuthal Inhomogeneous Heat Flux With Focus On Mixed Convection, Karlsruhe Institute of Technology, 2025, https://doi.org/10.35097/yqghfhjcbbybewqv.